JUPITER'S GREAT RED SPOT AND OTHER VORTICES

Philip S. Marcus

Department of Mechanical Engineering, University of California, Berkeley, California 94720

1. INTRODUCTION

Probably the question most frequently asked about the Great Red Spot (GRS) is "What is it?," as if a single powerful word or phrase—soliton, Taylor column, Rossby wave, hurricane—could neatly explain its 300 years of observation (Hook 1665, Cassini 1666) and modeling. The GRS is a nearly 2-dimensional vortex not attached to any topographic feature. Such vortices abound in Nature, but the peculiarities of the GRS, such as its huge size, persistent survival amid turbulence, and (most vexing from our point of view) why there is no terrestrial analog, are due to Jupiter's rapid rotation, nearly dissipationless atmosphere (no boundary layers), and strongly shearing east-west winds. This review argues that these three ingredients are essential for the formation and maintenance of the GRS, and that any flow having all three traits such as those found on Saturn, Neptune, and most other locations on Jupiter also have long-lived vortices.

We present a tutorial in vortex dynamics to explain theoretically the GRS as the self-organization of vorticity in turbulence. We avoid presenting models with enough free parameters to obtain a solution that reproduces exactly the GRS velocity and the motion of every cloud. The quality of the observations does not warrant it, and a misinterpretation of them can lead to incorrect conclusions. In the next section we list a number of properties of the GRS and the other Jovian vortices that are unambiguous from the data. The remainder of this paper develops the simplest possible model that explains these properties one at a time rather

523

than in an all-encompassing planetary global circulation model in which they are all present together, making interpetation and analysis difficult. Our equations are simple enough to understand each property in a physically intuitive way or with a back-of-the-envelope calculation, yet sufficiently complete to make quantitative predictions based on detailed numerical computations for future observations and laboratory experiments.

2. THE WEATHER LAYER

Jupiter has an equatorial radius of 71,400 km and is everywhere a fluid except for a small solid core (Stevenson 1982). However, in this review we are concerned only with the fluid dynamics in the thin weather layer that contains the visible cloud tops. Above and at the top of this layer the atmosphere is stably stratified and acts as an impermeable lid on the underlying, up-welling, convecting[1] fluid (which creates the visible condensates in the clouds). This layer is the only region where we can detect vortices (by using cloud motions and patterns), but because the layer is at the interface of the convecting and stable parts of the atmosphere its dynamics are unique. It may be the only Jovian layer where coherent vortices exist. Because the convection is weak and the planet's rotation (1 Jovian day = 9.92 h) is strong, the horizontal motions in the layer are approximately two-dimensional (i.e. independent of the vertical direction z) via the Taylor-Proudman theorem (Ghil & Childress 1987). However, the vertical convective velocity v_z from the underlying layer goes to zero in the weather layer, so $|\partial v_z/\partial z|$ is big. As shown in Section 3.1, two-dimensionality, rapid rotation, and large $|\partial v_z/\partial z|$ create strong, vortical, horizontal flows.

There has been much speculation about the vertical depth and structure of the GRS, including a suggestion that there is a counter-rotating vortex beneath it (Flierl et al 1983). The vertical scale height of the hydrogen-helium mixture in the weather layer is 22 km (Hunt 1983). Because numerical calculations of compressible convection indicate that coherent eddies usually do not extend more than one or two vertical scale heights, it is reasonable to assume that the depth of the Jovian vortices is 20–40 km. This depth is much less than the horizontal size of the GRS (26,000 × 13,000 km) and also less than the size of the smallest vortices resolved by *Voyager* (500 km in radius). It is this pancake-like structure of the vortices, that motivates our treatment of the weather layer as a thin shell rather than as a part of a star-like model that includes the entire planet.

---

[1] Jupiter's internal heating is estimated to be 2/3 that of its solar heating.

In addition to the vortices, the weather layer has approximately axisymmetric east-west winds. Their mean values v_{Lim} have been calculated by Limaye (1986) and are shown in Figure 1. The characteristic wind velocities at their extrema are ± 100 m s^{-1}. Although they are turbulent, their mean values changed little during the 5 months between the *Voyager 1* and *2* encounters. The colors of the approximately axisymmetric bands around Jupiter change on a 1–5 year time scale, but from Earth-based studies it does not appear that the variability of the color is tied to that of the velocities. (As shown in Section 6.3, cloud tracers can be deceiving.) It remains controversial how the observed v_{Lim} is related to the flow beneath the weather layer (cf Williams 1985), but it is generally agreed that the radiative time scale of the underlying flow is ~ 10 years which is long compared with the turnaround times of the vortices. The period of a tracer in the circumferential ring (Figure 2) around the GRS is much smaller and is 6–10 days. Thus, although the influence (or the boundary condition
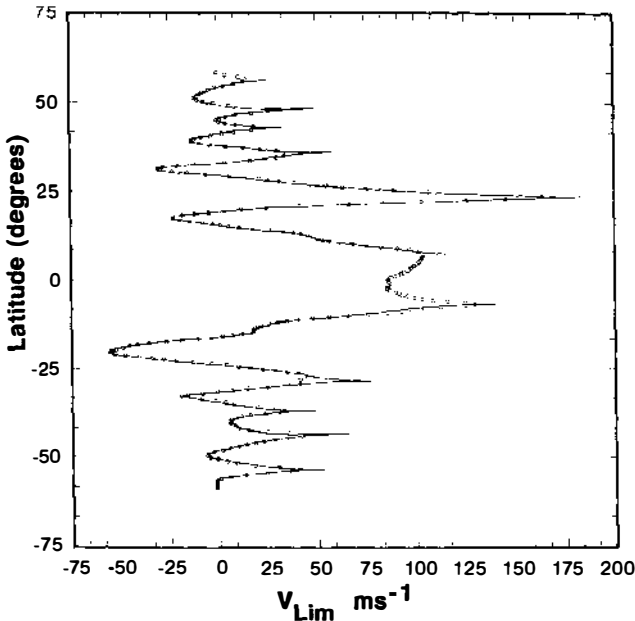
Figure 1 Latitudinal dependence of v_{Lim}. The circles are the mean, axisymmetric Jovian, east-west, zone-belt velocity v_{Lim} as determined by Limaye. The uncertainties are ± 7 m s^{-1}. The solid curve is a fit with discontinuities in the latitudinal derivative at the east-going extrema or band boundaries described in Section 10. The equatorial flow is not fit with a model because it is not geostrophic.
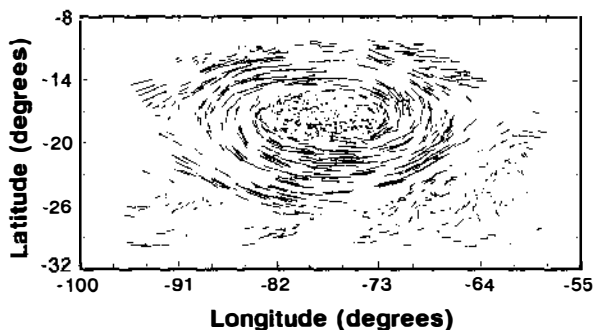
Figure 2 The 1161 cloud displacements of the GRS as determined by Beebe (1991) from *Voyager 1*. Most of the velocity and vorticity is in the circumferential ring of width $\sim 4° \simeq 4600$ km $\simeq 2L_r$. The peak velocity is in the northern GRS and is ~ 120 m s^{-1}, and the characteristic north-south velocity is 50 m s^{-1}. The uncertainty in each vector is 2-4 m s^{-1}.

imposed) upon the weather layer by the underlying layer is unknown, it is usually assumed to be constant in time. Regions where the shear of $\mathbf{v}_{Lim}$ is *cyclonic* (in the same direction as the planet's rotation, or clockwise in the Southern hemisphere) are defined as *belts* and those where it is anti-cyclonic as *zones*.

The GRS at 22.5°S is the largest Jovian vortex and is an anti-cyclone. Figure 3 shows that it has a quiet center and that most of its velocity and
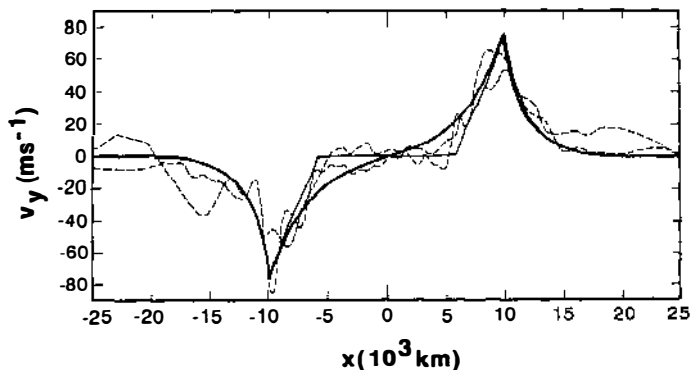

Figure 3 North-south velocities from *Voyagers 1* and *2* of the GRS along its east-west axis near 22.5°S (two *dashed curves*). The difference of the two curves, taken 126 days apart, indicates the unsteadiness of the flow. The heavy solid curve is the velocity of a one-contour, uniform-$\bar{q}$ model with $L_r = 2500$ km, and $\bar{q} = 7 \times 10^{-5}$ s^{-1}. The heavy curve shows a quiet vortex center with most of the ω in the circumferential ring of width $\sim 2L_r$—the hallmark of uniform-$\bar{q}$ vortices. The velocity of the two-contour model with critical value of $\bar{q}_1$ at the center as described in Section 6.2 is shown with the thin curve.

vorticity are in a thin circumferential ring at the outer edge of the vortex. Though it is presumed that the GRS has existed continuously since its first observation, its cloud pattern has been as large as 40,000 km and as small as 14,000 km in length, so its velocity may also have changed. Mac Low & Ingersoll (1986) identified over 100 Jovian vortices from the *Voyager* images, but they saw many vortex births, deaths, and mergers during their 58 days of observation, so it is not known how many vortices are truly long-lived. The major vortices other than the GRS are the three White Oval anti-cyclones at 33°S (whose births were witnessed in 1938–40), the chain of 12 cyclones and 12 anti-cyclones at 41°S (Figure 4), the Little Red Spot and brown and white anti-cyclones at 19°N, and the elongated cyclonic barges at 14°N. From the *Voyager* images, it is apparent that the vortices and their interactions are very turbulent.

The goals of the theory presented in this review are to explain how these vortices survive in the turbulent atmosphere, the role of v_{Lim} in maintaining them, why the vortices drift to the east or west, why there are more anti-cyclones than cyclones, where the vortices are located in latitude with respect to the extrema of v_{Lim}, what sets the scales for a vortex's size and velocity, what determines the shape of the vortices, how and why vortices merge together, what determines the number of vortices at a given latitude, why the clouds of cyclones are usually more filamentary than those of anti-cyclones, why the GRS is cooler at its interior than its outer edge, and why the GRS and the cyclonic barges have circumferential rings of high speed flow while the other vortices do not. This review treats these general questions rather than focusing on numerical simulations that try to reproduce the instantaneous GRS velocity determined from *Voyager* images.

Golitsyn (1970) was the first to propose that the GRS is a free vortex and not attached to a topographic feature such as a mountain. Read & Hide (1984) suggested that the GRS is strongly baroclinic, and they created a long-lived, anti-cyclone (accompanied by a weaker cyclone) in their laboratory by heating the inside and cooling the outside of a rapidly rotating annulus of water. However, the anti-cyclone existed only when the flow was laminar. Maxworthy & Redekopp (1976) examined the long-wavelength limit of the shallow-water equations to obtain the Korteweg-de Vries (KdV) and modified KdV equations. They proposed that the GRS is a soliton solution to these equations. Though they were able to create vortex solitons in the laboratory, the solitons did not mimic Jovian vortex interactions nor have the 2:1 elliptical shape of the GRS. Williams (1985) and Nezlin (1986) independently proposed that the GRS is a solitary wave solution to the intermediate-geostrophic (IG) equations. Their theory and experiments (Antipov et al 1982) have the attractive property that
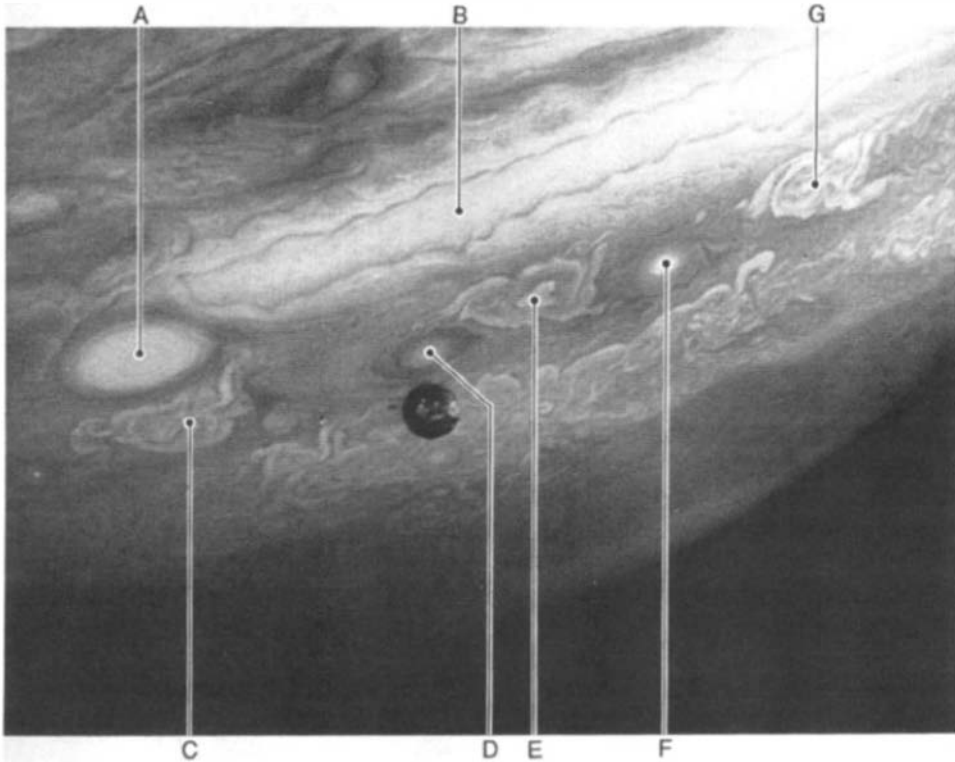
Figure 4   Voyager image centered near 41°S showing 3 cyclones (filamentary clouds at **C**, **E**, and **G**) just north of 2 anti-cyclones (bright elliptical clouds surrounded by dark rings at **D** and **F**). A full view at this latitude shows a Kármán vortex street of 12 cyclones staggered with 12 anti-cyclones. The anti-cyclones are centered in the zone south of the belt in which the cyclones are centered. The cyclones overflow their belt on the pole side and anti-cyclones overflow on the equator side, so they are all nearly at the same latitude. The anti-cyclones are ~600 km long. One of the three White Ovals at 33°S (**A**) is shown overflowing its zone on the equator side. The large, band-like cyclone (**B**) is one of three in the belt north of the Ovals. The round disk near the center is the moon Io.

anti-cyclones are preferred over cyclones, but they also predict that the vorticity of the GRS should be Gaussianly peaked at its center rather than in a circumferential ring. Ingersoll & Cuong (1981) argued that the GRS is quasi-geostrophic (QG) and maintains itself by merging with and absorbing smaller vortices. Marcus (1988a) and Sommeria et al (1988) also studied QG vortices and showed that the east-west winds were essential for maintaining them in a turbulent flow. This review focuses on QG vortices. We refer the reader to the review articles by Williams (1985) for more complete descriptions of IG Jovian models, by Beebe et al (1989) for the

observations of Jovian vortices, and by Ingersoll (1991) for more general discussions of the Jovian atmosphere.

3.   QUASI-GEOSTROPHIC APPROXIMATION

Here, we sketch the physical motivation for the QG equations and list the assumptions under which they are valid. We also introduce a nonstandard decomposition for the velocity and its governing equation so that the reader can easily gain an intuitive understanding of QG solutions.

3.1   One-Layer, Shallow-Water Equations

When considering fluid motions in a thin shell of an atmosphere whose vertical (with respect to the local direction of gravity) extent is much smaller than its horizontal, it is common to model the shell as a coupled set of immiscible thin layers and to ignore the remainder of the atmosphere above and below the shell of interest. The interactions of the fluid in the shell with the remainder as well as the heating from the sun and planetary core are modeled with artificial vertical boundary conditions. When the horizontal length of the region of interest is small with respect to the mean radius of the shell, the spherical geometry is replaced with a simpler flat approximation where y is the north-south and x the east-west coordinate. (Or in an annular geometry, polar coordinates r and ϕ as the latitude and longitude are used.) The simplest model has only a single layer of constant density with mean depth H_0 and has an upper boundary that acts as a free surface: Waves of height $h(x, y, t)$ deform it from its unperturbed location. When the density of the atmosphere increases rapidly with depth so that the fluid below the shell has large inertia and is not affected by the motions in the shell, the bottom boundary is approximated as rigid so that the normal component of the velocity vanishes at a depth $[h_b(x, y) - H_0]$ below its unperturbed free surface. Thus the single layer of fluid has a total thickness of $H \equiv H_0 + h(x, y, t) - h_b(x, y)$. Often the depth $[h_b(x, y) - H_0]$ is not the location of a physical surface, but is a parameterization of the influence of the underlying layer. This approximation is crude but works well for many atmospheric and oceanographic problems, especially when 1. the characteristic vorticity of the flow is small compared with the angular velocity of the rotating planet, 2. the Eulerian time scales are of the same order or longer than the advective time scales, 3. the Brunt-Väisällä frequency of the fluid in the shell is real (i.e. the fluid is stable to convection) and nearly independent of depth, 4. the baroclinic forces are small (i.e. the surfaces of constant pressure and density are nearly coincident), and 5. the horizontal scales are very much longer than the vertical.[2] The model is

---

[2] Some, but not all, of these conditions are required. For example, a layer with horizontal length and width of the same order is often well-approximated by the shallow-water equations if the flow is rapidly rotating.

called the one-layer, shallow-water approximation, and its asymptotic derivation and the assumed scalings are in standard texts (cf Ghil & Childress 1987).

Using this approximation, the horizontal component of the momentum equation as viewed in the rotating frame of a planet is

$$\frac{D\mathbf{v}}{Dt} \equiv \frac{\partial \mathbf{v}}{\partial t} + (\mathbf{v} \cdot \nabla \mathbf{v}) = -g\nabla h + f(y)\mathbf{v} \times \hat{\mathbf{z}}, \tag{1}$$

where g is the reduced acceleration of gravity,[3] $\hat{\mathbf{z}}$ is the unit vector in the local vertical direction, and $f(y)$ is the coriolis parameter which is defined to be twice the magnitude of the planet's angular velocity component in the $\hat{\mathbf{z}}$ direction. [Thus $f(y)$ is a function of latitude and is zero at the equator.] Note that we have assumed that horizontal velocity $\mathbf{v}$ is independent of z. Equation (1) is the dissipationless Euler equation in a rotating frame for a two-dimensional fluid except that $g\nabla h$ has replaced the usual term of the pressure gradient divided by density, and f is not constant. The remaining equation that governs the dynamics is the continuity or mass-conservation equation. By combining it with the curl of Equation (1) it can be written as (Ghil & Childress 1987):

$$\frac{D}{Dt}\left(\frac{\omega(x, y, t) + f(y)}{H}\right) = 0, \tag{2}$$

where $\omega(x, y, t) \equiv (\nabla \times \mathbf{v}) \cdot \hat{\mathbf{z}}$ is the vertical component of the vorticity. In this paper we define the quantity $q \equiv H_0[\omega(x, y, t) + f(y)]/H$ as the potential vorticity, and Equation (2) shows that it is advectively conserved.

To get some feel for Equation (2), consider an infinitesimal column of fluid (where the horizontal boundary of the column is defined by a sheet of passively advected blue dye extending from the bottom to top boundary). As the column moves, the shape of its boundary and its area change. Let H be constant. Then, as the column changes its latitude, $f(y)$ changes, so $\omega(x, y, t)$ must change appropriately for q to remain constant, and the column spins up or down. If H is not constant and if the column moves along a line of constant latitude but into a thicker part of the layer, then $|f + \omega(x, y, t)|$ must increase. The classic example of this is the "drain in the sink effect" (of which everyone learns, but no one actually observes due to much greater frictional forces and uncooperative initial conditions). It

---

[3] The reduced g is the gravity multiplied by the local buoyancy of the fluid. For example, if the layer had constant density ρ and lay above one with density $\rho + \Delta\rho$ then the gravity would be multiplied by $\Delta\rho/\rho$. If it were neutrally buoyant (i.e. neutrally stable to convection) then g would be zero.

occurs when a column of fluid approaches and then goes down the drain of a sink on a rotating Earth. As the fluid goes down the drain H rapidly increases, so $|f(y) + \omega|$ must increase. The vorticity $\omega(x, y, t)$ as observed in the rotating frame increases in the Northern hemisphere and decreases in the Southern. This effect can be represented by adding the forcing term, $(q/H_0)(\partial v_z/\partial z)$ to the right hand side of Equation (2). The forcing can be large even when v_z is small compared to the horizontal velocity.

3.2   Eulers Equation—Constant f and H

When f and H are constant, Equation (2) reduces to the curl of Euler's equation

$$D\omega/Dt = 0, \tag{3}$$

and it is worthwhile to obtain some understanding of this equation's solutions such as the single point vortex of circulation Γ: $\omega(x, y, t) = \Gamma\delta(x - x_0)\delta(y - y_0)$. The velocity due to its vorticity is found by inverting the curl operator using the Biot-Savart law in a way that is completely analogous to the way the magnetic field is obtained from an electric current. In a cylindrical coordinate system with origin at the guiding center (x_0, y_0): $v_r = 0$ and $v_\phi(r) = \Gamma/2\pi r$. Thus a point vortex creates an axisymmetric azimuthal velocity about itself with a strength that falls off inversely with distance. The guiding center moves with the velocity of the local flow, and Γ is conserved. For a single point vortex the velocity at the vortex itself is zero, so there is no self-advection, and the vortex remains at rest. A collection of N point vortices with

$$\omega(x, y, t) = \sum_{i=1}^{N} \Gamma_i \delta[x - x_i(t)]\delta[y - y_i(t)] \tag{4}$$

is also a solution to (3) where the circulations of the vortices Γ_i remain constant and where the guiding centers of each vortex $[x_i(t), y_i(t)]$ move with the local velocity (Chorin 1993). The velocity is a linear function of the vorticity, so it is equal to the superposition of the contributions calculated from each delta function by use of the Biot-Savart law. For example, two point vortices of the same sign rotate about their center-of-vorticity, while a dipolar pair of vortices with strengths $\pm\Gamma$ and separation d advect as a coherent unit in a direction perpendicular to the line between them and at a velocity of $\Gamma/2\pi d$. The N-body point vortex problem has no general closed-form solution, but in an unbounded flow the circulation, linear momenta, angular momentum, and energy of N point vortices or a

continuous distribution of vorticity $\omega(x, y, t)$ are all conserved in time. (See Section 3.5.)

3.3 Standard QG Equations—an Advectively Linear Decomposition

Of course, it is much simpler to develop an intuition for the solutions to Equation (3) than to the full one-layer, shallow-water Equations (1)–(2). In part this is because Equation (3) is *advectively* linear: The quantity that is advected, in this case ω, is linearly related to **v**. Therefore the velocity due to each infinitesimal patch of vorticity can be linearly superposed even though Equation (3) is itself nonlinear in **v** due to the D/Dt operator. Fortunately Equation (2) can be made advectively linear by using the standard quasi-geostrophic (QG) approximation (cf Ghil & Childress 1987). The usual advantage of the QG approximation is that it makes solutions easier to find analytically or compute numerically, but here we employ it for pedagogical reasons: It makes the solutions easier to interpret physically. The QG approximation assumes the scaling: $\langle v \rangle / \langle l \rangle \langle f \rangle = \langle \omega \rangle / \langle f \rangle = O(\varepsilon)$, $\langle h_b \rangle / H_0 \leq O(\varepsilon)$, $\langle h \rangle / H_0 \leq O(\varepsilon)$, $\langle f_0 - f(y) \rangle / f_0 \leq O(\varepsilon)$, and $\langle \tau \rangle \langle v \rangle / \langle l \rangle \geq O(1)$, where the notation $\langle \ \rangle$ means "average value of," $\langle \tau \rangle$ is the characteristic Eulerian time over which h and **v** change, $\langle l \rangle$ is the characteristic horizontal length over which they change, f_0 is the average value of $f(y)$ at the latitude of interest, and ε is the Rossby number and assumed small. In Section 11 we examine the validity of this approximation and other scalings, such as those used in the IG equations, to the Jovian weather layer.

To leading order in ε, the QG momentum Equation (1) becomes the kinematic geostrophic balance equation:

$$\mathbf{v} = \hat{\mathbf{z}} \times \nabla \left(\frac{gh}{f_0} \right) \equiv \hat{\mathbf{z}} \times \nabla \psi. \tag{5}$$

So in the QG approximation $(\nabla \cdot \mathbf{v}) \equiv 0$, and **v** is derivable from the stream function $\psi \equiv gh/f_0$. The equation for the potential vorticity (2) becomes

$$\frac{D}{Dt} \left\{ \omega + [f(y) - f_0] - \frac{h f_0}{H_0} + \frac{h_b(x, y) f_0}{H_0} \right\} =$$

$$\frac{D}{Dt} \left\{ \nabla^2 \psi - \frac{\psi}{L_r^2} + \frac{h_b(x, y) f_0}{H_0} + [f(y) - f_0] \right\} = 0, \tag{6}$$

where we have used $\omega = \nabla^2 \psi$ and defined the Rossby deformation radius as $L_r \equiv (\sqrt{gH_0})/|f_0|$. In the QG approximation $q \equiv \nabla^2 \psi - (\psi/L_r^2) + [h_b(x, y) f_0$

3.4 Decomposed QG Equations—Advectively Linear and Homogeneous

Equation (6) is advectively linear but inhomogeneous. To make its solutions more intuitive we recast it in a homogeneous form by breaking the velocity into the sum of a time-independent and x-independent zone-belt part $\bar{\mathbf{v}} = \bar{v}_x(y)\hat{\mathbf{x}}$ and a time-dependent remainder $\tilde{\mathbf{v}}(x, y, t) \equiv \mathbf{v}(x, y, t) - \bar{\mathbf{v}}$. The $\bar{\mathbf{v}}$ is determined from its stream function $\bar{\mathbf{v}}(y) \equiv \hat{\mathbf{z}} \times \nabla\bar{\psi}(y)$ with $\bar{\psi}(y)$ defined by

$$\left(\nabla^2 - \frac{1}{L_r^2}\right)\bar{\psi}(y) \equiv \bar{q} - h_b(y)f_0/H_0 - [f(y) - f_0], \tag{7}$$

where $\bar{q}$ is an arbitrary constant (and is equal to the potential vorticity of the flow when $\mathbf{v} = \bar{\mathbf{v}}$) and where we have assumed that h_b is a function only of y. From (7), $\bar{\psi}$ is unique up to three degrees of freedom: two integration constants and the choice of $\bar{q}$. Once these three constants are chosen and $\bar{\psi}$ is known, all of the other variables are defined and decomposed in the obvious way: $\tilde{\mathbf{v}}(x, y, t) \equiv \hat{\mathbf{z}} \times \nabla\tilde{\psi}(x, y, t)$, $\bar{\omega}(y) \equiv \nabla^2\bar{\psi}(y)$, $\tilde{\omega}(x, y, t) \equiv \nabla^2\tilde{\psi}(x, y, t) = \omega - \bar{\omega}$, and $\tilde{q}(x, y, t) \equiv \nabla^2\tilde{\psi}(x, y, t) - \tilde{\psi}(x, y, t)/L_r^2 = q - \bar{q}$.

Because $\bar{q}$ is constant, Equation (6) becomes both advectively linear and homogeneous in $\tilde{q}$:

$$\frac{D\tilde{q}}{Dt} = \left[\frac{\partial}{\partial t} + (\tilde{\mathbf{v}} \cdot \nabla) + \tilde{v}\frac{\partial}{\partial x}\right](\nabla^2\tilde{\psi} - \tilde{\psi}/L_r^2) = 0. \tag{8}$$

This decomposition is just a mathematical trick and is always valid, but it is most pedagogically useful for flows on Jupiter if the mean zone-belt flow found by Limaye $\mathbf{v}_{\text{Lim}}(y)$ has roughly (to order ε) uniform potential vorticity so that it is represented by $\bar{\mathbf{v}}$. In that case, $\tilde{\mathbf{v}}(x, y, t)$ represents the coherent vortices, the turbulent component of the flow, the departures of $\mathbf{v}_{\text{Lim}}(y)$ from $\bar{\mathbf{v}}$, and the Rossby waves (which need a ∇q). Or equivalently, the decomposition is most useful when $\tilde{q}(x, y, t)$ has nontrivial values only in a few compact regions of the flow. Whether $\mathbf{v}_{\text{Lim}}(y)$ has approximately uniform q is discussed in Sections 10 and 11. Clearly, when $\bar{\mathbf{v}} = \mathbf{0}$ and $L_r \to \infty$, Equation (8) reduces to Equation (3). When polar rather than Cartesian coordinates are used in the quasi-geostrophic equations we decompose the flow so that the zone-belt component is in the azimuthal direction and a function only of r.

Equation (8), which governs the dynamics of $\tilde{\mathbf{v}}$ rather than $\mathbf{v}$, has solutions that are analogous to the point-vortex solutions of Euler's equation.

For any $\bar{v}$ and L_r, it is satisfied by a collection of N point *potential* vortices of strength $\tilde{\Gamma}_i$:

$$\tilde{q}(x, y, t) = \left(\nabla^2 - \frac{1}{L_r^2}\right)\tilde{\psi} = \sum_{i=1}^{N} \tilde{\Gamma}_i \delta[x - x_i(t)]\delta[y - y_i(t)]. \tag{9}$$

The stream function due to $\tilde{q}$ is found by inverting the Helmholtz operator in Equation (9):

$$\tilde{\psi}(x, y, t) = -\frac{1}{2\pi}\sum_{i=1}^{N} \tilde{\Gamma}_i K_0\left\{\frac{\sqrt{[x - x_i(t)]^2 + [y - y_i(t)]^2}}{L_r}\right\} \tag{10}$$

where K_v is the vth-order modified Bessel function bounded at ∞ (and the Greens function of the Helmholtz operator). The velocity $\tilde{v}$ is the linear superposition of the velocity around each point potential vortex which is azimuthal around each guiding center and falls off as $K_1(r/L_r)$ where r is the distance from the vortex. (When L_r is infinite, K_0 is replaced by $-\ln$ in Equation 10.) For distances smaller than L_r, $K_0(r/L_r)$ behaves like $-\ln(r/L_r)$ and $K_1(r/L_r)$ like L_r/r, but for distances much larger than L_r both K_0 and K_1 fall off as $(\sqrt{L_r/r})e^{-r/L_r}$. Thus, just as the Debye length in a plasma screens a point charge so that the electric field is exponentially small at large distances, the Rossby deformation radius, L_r, screens a potential vortex so that the velocity is exponentially small at large distances.

The guiding center of each potential vortex moves with the total velocity v which is the linear sum of $\bar{v}$ and the velocities produced by the N potential vortices. So as in the case of infinite-L_r, when $\bar{v} = 0$ a single point potential vortex does not move, and two potential vortices with the same sign rotate around their center of potential vorticity while a dipolar pair advects as a coherent unit.

3.5   *QG Conservation Laws*

A collection of N potential point vortices as well as a flow with a continuous distribution of $\tilde{q}$ has several quantities conserved by Equation (6). If $\bar{v}$ is in the x direction and if the domain is unbounded or has rigid boundaries in the y direction and periodic boundaries in the x direction, then the conserved potential circulation is

$$\tilde{\Gamma} = \sum_{i}^{N} \tilde{\Gamma}_i = \int \tilde{q}(\mathbf{r}) d^2r. \tag{11}$$

The x-component of the momentum is conserved and is (up to multiplicative and additive constants) just the $\tilde{q}$-weighted value of y:

$$P_x = \sum_i^N \tilde{\Gamma}_i y_i(t) = \int y\tilde{q}(\mathbf{r}, t)\, d^2r. \tag{12}$$

For $\bar{v}_x \neq 0$, P_y is not conserved. If $\bar{\mathbf{v}}$ is in the azimuthal direction and the domain is unbounded or has annular or cylindrical boundaries, then the angular momentum about the origin is conserved and is (up to multiplicative and additive constants) just the $\tilde{q}$-weighted value of r^2:

$$L = -\frac{1}{2}\sum_i^N \tilde{\Gamma}_i|\mathbf{r}_i(t)|^2 = -\frac{1}{2}\int r^2 \tilde{q}(\mathbf{r}, t)\, d^2r. \tag{13}$$

When $\bar{\mathbf{v}} = \mathbf{0}$ and when the domain is unbounded, the angular momentum around any point, not just the coordinate origin, is conserved.

The conserved energy is a sum of two pieces (up to multiplicative and additive constants): (a) the self-energy, which is the kinetic and potential energy of the interaction of $\tilde{\mathbf{v}}$ with itself

$$\begin{aligned} E_{\text{self}} &= -\frac{1}{2}\sum_i^N \sum_{j \neq i}^N \tilde{\Gamma}_i \tilde{\Gamma}_j G\left(\frac{|\mathbf{r}_i(t) - \mathbf{r}_j(t)|}{L_r}\right) \\ &= -\frac{1}{2}\iint \tilde{q}(\mathbf{r}, t)\tilde{q}(\mathbf{r}', t)G\left(\frac{|\mathbf{r} - \mathbf{r}'|}{L_r}\right) d^2r\, d^2r' \end{aligned} \tag{14}$$

or

$$E_{\text{self}} = -\frac{1}{2}\int \tilde{q}(\mathbf{r}, t)\tilde{\psi}(\mathbf{r}, t)\, d^2r \tag{15}$$

and (b) the interaction energy which is due to the interaction of $\tilde{\mathbf{v}}$ and $\bar{\mathbf{v}}$

$$E_{\text{int}} = -\sum_i^N \tilde{\Gamma}_i \bar{\psi}(y_i) = -\int \tilde{q}(\mathbf{r}, t)\bar{\psi}(y)\, d^2r. \tag{16}$$

where G is the Greens function: $-(1/2\pi)K_0$ for finite and $1/2\pi \ln$ for infinite L_r.

4.   FINITE L_r: SLOWLY ROTATING VORTEX CENTERS

When $f = f_0$ any steady, axisymmetric $\mathbf{v}$ with $v_r = 0$ is a solution to the QG Equation (8). Consider a circular vortex with uniform potential vorticity of

strength $\tilde{q}$ and with potential circulation $\tilde{\Gamma}$, radius R, and $\bar{\mathbf{v}} = \mathbf{0}$. In cylindrical coordinates with origin at the vortex center

$$\tilde{q}(r) = \begin{cases} \tilde{\Gamma}/\pi R^2 & \text{for } 0 < r < R \\ 0 & \text{for } R \leq r. \end{cases} \tag{17}$$

The velocity produced by the vortex is $v_r = 0$,

$$\tilde{v}_\psi(r) = \begin{cases} \dfrac{\tilde{\Gamma}}{\pi R} K_1\left(\dfrac{R}{L_r}\right) I_1\left(\dfrac{r}{L_r}\right) & \text{for } 0 < r < R \\[2mm] \dfrac{\tilde{\Gamma}}{\pi R} I_1\left(\dfrac{R}{L_r}\right) K_1\left(\dfrac{r}{L_r}\right) & \text{for } R \leq r \end{cases} \tag{18}$$

and the vorticity is

$$\tilde{\omega}(r) = \begin{cases} \dfrac{\tilde{\Gamma}}{\pi RL_r} K_1\left(\dfrac{R}{L_r}\right) I_0\left(\dfrac{r}{L_r}\right) & \text{for } 0 < r < R \\[2mm] -\dfrac{\tilde{\Gamma}}{\pi RL_r} I_1\left(\dfrac{R}{L_r}\right) K_0\left(\dfrac{r}{L_r}\right) & \text{for } R \leq r, \end{cases} \tag{19}$$

where I_v is the vth-order modified Bessel function bounded at the origin. The velocity $\tilde{v}_\phi$ and vorticity are both small near the origin and have the same sign as $\tilde{q}$. They both increase exponentially in r with e-folding length L_r. Their magnitudes peak at the edge of the potential vortex at $r = R$. For larger r, $|\tilde{v}_\phi|$ exponentially decreases to zero. At $r = R$, $\tilde{\omega}$ is discontinuous, increases or decreases by $|\tilde{q}|$, and changes sign. As r increases, $|\tilde{\omega}|$ decreases exponentially back to zero.

Thus a signature of a vortex with uniform potential vorticity and radius greater than L_r is that it has a quiet center with most of its vorticity and velocity concentrated in a thin circumferential ring at its outer edge. The width of the ring is $2L_r$. The inner half of the ring has $\tilde{\omega}$ with the same sign as $\tilde{q}$ while the outer half has the opposite sign. Numerical solutions of Equation (6) with $\bar{\mathbf{v}} \neq \mathbf{0}$, and nonconstant f, such as those in Figure 3, also have this circumferential ring of width $2L_r$ as long as the $\tilde{q}$ within the vortex is approximately constant and $L_r \ll R_x$, where R_x is the major (east-west) semi-diameter of the vortex. Like the vortices in Equations (17)–(19), the ratios of $|\tilde{\omega}|$ and $|\tilde{v}_\phi|$ at the inner edges of the ring to the values near the vortex centers scale roughly as e^{R_x/L_r}. From Equation (19) it is apparent that vortices with $L_r \geq R_x$ have nearly uniform $\tilde{\omega}$ (which is equal to $\tilde{q}$ in the limit $L_r/R_x \to \infty$) throughout rather than concentrated at the edge, and they rotate as nearly solid bodies. These characteristics are

important because numerical simulations show that, at least to a first approximation, large vortices created by the merger of many small-area vortices have nearly uniform $\tilde{q}$.

The ring-like distributions of ω and circumferential velocity of QG, finite-L_r, approximately-uniform-$\tilde{q}$, potential vortices have been invoked to understand the $\mathbf{v}$ and ω in the GRS (Marcus 1988a). The quiet center and concentration of velocity into a circumferential ring (at $x = \pm 10,000$ km from the vortex center) are clearly seen in Figures 2 and 3 of the GRS. The vorticity is zero, to within the observational uncertainties, at the center of the GRS.[4] It rises to its peak value of 3×10^{-5} s^{-1} at the inside edge of the circumferential ring; quickly drops to zero half-way through the ring; reaches its most negative value of -3×10^{-5} s^{-1} at the outer edge of the ring; and then quickly decays to zero outside the GRS. The large cyclonic barge at 14°N also has a high speed circumferential ring (Hatzes et al 1981). Prior to 1988 there had been no attempt by theorists to explain the striking and unexpected departure of the GRS and the barge from solid body rotation, and it was largely ignored. Even after *Voyager* observations showed that the vorticity and circumferential velocity of the GRS increased rapidly away from its center, its exponential dependence on distance was not appreciated as shown by the fact that attempts were made to fit the circumferential velocity with a fourth-order polynomial over distances of $10L_r$ (Mitchell et al 1981)—an impossible task if the velocity exponentiates with scale L_r. A fit of the same velocity from the GRS center to the middle of the ring using an exponential rather than a polynomial is much better and gives an e-folding length of 2200 km (Marcus 1988a). An estimate of L_r at the GRS based on the dominant length of the local waves gives $L_r = 2000$ km (Williams & Yamagata 1984). The GRS has $R_x \simeq 13,000$ km, and the barge has $R_x \simeq 3800$ km. (Its local value of L_r is unknown.) Thus the exponential nature of the velocity in the GRS interior and the concentration of ω and $\mathbf{v}$ into a ring in both the GRS and the barge are consistent with them being large (i.e. $R_x \gg L_r$) QG potential vortices. Turning the problem around and assuming that the GRS is QG, has exactly uniform q, and is north-south symmetric (the last two assumptions are much riskier), gives $L_r \simeq 1300$ km from a best fit to the observed velocity along its east-west axis (Marcus 1988a), and gives $L_r \simeq 2500$ km from the best fit over the entire GRS (see Figure 3). On the other hand by identifying the half-width of the ring of circumferential velocity around the GRS as L_r, we obtain $L_r \simeq 2300$ km (Marcus & Van Buskirk 1993), and since the width of a QG ring is so insensitive to all of

---

[4] R. F. Beebe (1993, private communication) has recently reported small positive values of ω at some locations near the center.

the other parameters, we shall use this value throughout the remainder of the paper.

The White Oval BC at 33°S has $R_x \simeq 5000$ km and $L_r \simeq 1600$ km. (Note that $L_r \propto 1/f(y)$ if gH_0 is independent of latitude.) Like a QG vortex with $R_x/L_r \simeq 3$, its vorticity is much more uniform throughout the vortex than the GRS and it rotates much more like a solid body.

It should be noted that the predicted distribution of vorticity within the GRS is one way in which current theories of the GRS differ substantially. In particular, the intermediate-geostrophic (IG) theory proposed by Williams (1985) and Antipov et al (1982) produces soliton-like vortices that are always characterized by a Gaussian distribution of ω peaked at the vortex center. They never have the vorticity or circumferential velocity peak at the outer edge like QG vortices or the GRS. Although QG and IG vortices differ in many ways (see Section 11) this is the most striking feature.

5.   QG VORTICES GO WITH THE FLOW

The guiding center of a point potential QG vortex moves with the local velocity, and a finite-area patch of potential vorticity moves with the local velocity averaged over its area. To see this, define X, the local $\tilde{q}$-weighted average value of x, to be the vortex's location in x:

$$X \equiv \frac{\int \tilde{q}(\mathbf{r}) x \, d^2 r}{\int \tilde{q}(\mathbf{r}) \, d^2 r}, \tag{20}$$

where the integral is over the boundary of the patch which is defined to be any closed contour of constant $\tilde{q}$. The velocity of the patch in the x direction is $U_x \equiv dX/dt$. Differentiating (20) gives

$$U_x = \frac{\int \tilde{q}(\mathbf{r}) v_x \, d^2 r}{\int \tilde{q}(\mathbf{r}) \, d^2 r}, \tag{21}$$

where we have used Equation (8), the fact that the boundaries of the integrals are Lagrangian contours, and the fact that $(\nabla \cdot \mathbf{v}) = 0$. An equation similar to (21) holds for the y coordinate and shows that the patch advects with the local $\tilde{q}$-weighted average value of v_y. Equation (21) can also be written as

$$U_x = \bar{U}_x + \frac{\int \tilde{q}(\mathbf{r})\tilde{v}_x \, d^2r}{\int \tilde{q}(\mathbf{r}) \, d^2r} = \bar{U}_x + \frac{\oint \tilde{v}_x(\tilde{\mathbf{v}} \cdot d\mathbf{s}) - \frac{1}{2}\oint(|\tilde{\mathbf{v}}|^2 + \tilde{\psi}^2/L_r^2)(\hat{\mathbf{x}} \cdot d\mathbf{s})}{\int \tilde{q}(\mathbf{r}) \, d^2r}$$

(22)

where

$$\bar{U}_x \equiv \frac{\int \tilde{q}(\mathbf{r})\bar{v}_x \, d^2r}{\int \tilde{q}(\mathbf{r}) \, d^2r}$$

(23)

is the local $\tilde{q}$-weighted average value of $\bar{v}_x$. The surface terms in Equation (22) represent the advection due to the neighboring patches and the boundaries. If the patch is separated from other patches and the boundaries by distances greater than L_r, then the surface terms are exponentially small and easily approximated: They are the superposition at the patch center of the velocities due to the nearby patches (which are treated as point potential vortices) and the boundaries (which are replaced by image point vortices). Thus the patch moves at a velocity $\mathbf{U}$ approximately equal to $\bar{U}_x\hat{\mathbf{x}}$ plus a small correction due to the velocity from local point potential vortices (found from the $\tilde{\psi}$ in Equation 10). When the flow is unbounded and consists of one isolated patch of $\tilde{q}$ with $\tilde{q} = 0$ outside the patch, then regardless of the shape of the patch $\mathbf{U} \cong \bar{U}_x\hat{\mathbf{x}}$. To see this: Take the integrals in Equations (20)–(23) over the entire domain so that the surface integrals in (22) vanish. Taking the integrals in (23) over the full domain is equivalent to taking them over just the patch.

The observed mean velocities $\mathbf{U}^{obs}$ of the long-lived Jovian vortices agree with the QG velocities predicted from Equation (21); $U_y^{obs} \simeq 0$, and U_x^{obs} agrees with U_x to within the expected uncertainties. The uncertainties in U_x^{obs} are less than 1 m s^{-1}; however, those in U_x are large due to the 25% uncertainty in measuring $\tilde{q}(x, y, t)$. (See Section 11.) For the GRS, U_x can be found directly from Equation (21) and is -1 ± 8 m s^{-1} while $U_x^{obs} = -3.5$ m s^{-1}. Jovian vortices other than the GRS and White Ovals are sufficiently small and north-south symmetric that their values of U_x are nearly equal to v_x at the vortex center. So, assuming $v_x(y) = \mathbf{v}_{Lim}$ at the vortex center (plus corrections that are linear or odd in y), and assuming that the center of the vortex is the same as the center of the clouds associated with it, QG theory predicts that a small vortex moves at the local Limaye velocity. (This reasoning is valid even if the q of $\mathbf{v}_{Lim}$ is not

uniform.) We argue that the errors in these assumptions coupled with the error in determining the center of the clouds is less than or equal to the ± 7 m s^{-1} uncertainty in $\mathbf{v}_{\text{Lim}}$, so for small QG vortices, $\mathbf{U} = \mathbf{v}_{\text{Lim}} \pm 7$ m s^{-1}. In contrast, IG theory predicts that vortices move west at the local Rossby long-wave speed of $-\beta L_r^2$ (Williams 1985) where β is the local gradient of $f(y)$. The IG vortex speed is $-4.6(L_r/1000 \text{ km})^2$ m s^{-1} for the GRS, $-5.4(L_r/1000 \text{ km})^2$ m s^{-1} for the Little Red Spot (an anti-cyclone at 19.2°N with $U_x^{\text{obs}} = -2.5$), and $-3.9(L_r/1000 \text{ km})^2$ m s^{-1} for the White Oval BC (with $U_x^{\bullet\text{bs}} = +4$ m s^{-1}, i.e. east not west). Thus assuming that $L_r > 2000$ km, IG theory predicts that the speed of the GRS is to the west and greater than 18.4 m s^{-1}. To make IG theory consistent with observations, Williams & Wilson (1988) proposed that an ad hoc external, north-south forcing term (perhaps due to the influence of an underlying layer) should be added to the shallow-water momentum Equation (1). They determined that the term would have to produce an ageostophic east-west velocity of 10 m s^{-1}—a large correction, considering the fact that for the small spots $\langle v \rangle = 10$ m s^{-1} and $\langle U_x^{\text{obs}} \rangle = 5$ m s^{-1}.

It should be noted that in addition to their time-averaged, east-west velocities, some Jovian vortices also have slow, large amplitude, east-west oscillations. The GRS has both a 90 day (Smith & Hunt 1976) and a 50 year period, and the three White Ovals also slowly oscillate. These slow motions are probably due to the interactions with other Jovian vortices via the surface terms in Equation (22) and are discussed in Section 10.

6.   BREAKING PROGRADE/ADVERSE DEGENERACY

6.1   *Expulsion of Adverse Vorticity*

The potential vorticity $\tilde{q}$ and the local zone-belt shear $\bar{\sigma}(y) \equiv -\partial \bar{v}_x/\partial y$ or $\bar{\sigma}(r) \equiv r(\partial \bar{v}_\phi/r)/\partial r$ are defined as *adverse* if they have the opposite sign; otherwise, they are *prograde*. Numerical calculations show that vortices embedded in prograde and adverse shear behave differently. Adverse vortices with $|\bar{\sigma}/\tilde{q}| \geq O(1)$ at their centers are stretched by $\bar{v}$ into thin filaments which either fragment into many small pieces that scatter throughout the flow, decay if they become thinner than the dissipative length scale (in numerical computations of Equation 6 a dissipation is usually added), or are driven out of the local belt or zone. Prograde potential vortices with $\bar{\sigma}/\tilde{q} \geq O(1)$ evolve to equilibria that are approximately elliptical with their major axes aligned with $\bar{v}$. Figure 5 shows an example of both effects in an annular geometry where $\bar{v} = \bar{v}_\phi(r)\hat{\phi} = \{-r^2/6[2+(\bar{r}/r)^3]+0.48r\}\hat{\phi}$, so $\bar{\sigma}(r) = r/3[(\bar{r}/r)^3 - 1]$, where $\bar{r}$ is the latitude midway between the inner

$R_{in} \equiv 1/3$ and outer $R_{out} \equiv 4/3$ boundaries. This $\bar{\mathbf{v}}$ crudely represents a cyclonic belt with $\bar{\sigma}(r) > 0$ for $r < \bar{r}$, and an anti-cyclonic zone with $\bar{\sigma}(r) < 0$ for $r > \bar{r}$. (Without loss of generality we have let $f > 0$.) Initially the belt and zone in Figure 5a each contain one prograde and one adverse vortex, with light regions corresponding to $\tilde{q} > 0$, dark to $\tilde{q} < 0$, and gray to $\tilde{q} = 0$. In each case the adverse vorticity is initially expelled outward in a spiral from the center of its initial zone or belt (Figure 5b). Part is stretched to the small scales where it produces Kelvin-Helmholtz waves (as in the inner dark vortex in Figures 5c and 5d) and part is flung into the neighboring belt or zone where it suddenly, upon crossing $r = \bar{r}$, becomes prograde and forms tadpole-like heads (Figures 5d and 5e). The two new prograde vortices settle into a quasi-stable equilibrium with the long spiral white tail in Figure 5f dissipating. In contrast the two initial prograde vortices barely change. (Eventually the two light prograde vortices in Figure 5f merge.)

To understand why adverse $\tilde{q}$ spirals outward to the zone-belt boundaries, consider the schematic in Figure 6 showing a part of Figure 5a. The figure is in the frame of reference where the center of potential vorticity of the shaded vortex is at rest, so $\bar{\mathbf{v}}(r)$ is approximately zero at its center. An infinitesimal piece of $\tilde{q}$ labeled A at the lower edge of the vortex moves with $\mathbf{v}(\mathbf{r}, t) \equiv \tilde{\mathbf{v}}(\mathbf{r}, t) + \bar{\mathbf{v}}(r)$. The Biot-Savart law gives $\tilde{\mathbf{v}}$ (shown with thin solid arrows); it is clockwise around the vortex, and at A, $\tilde{v}_\phi \simeq -\tilde{q}R_r/2$ (or less, if $R_r \gg L_r$) where R_r is the vortex semi-radius in r. Taylor expansion of $\bar{\mathbf{v}}$ around the vortex center gives $\bar{\mathbf{v}}$; at A, $\bar{v}_\phi \simeq R_r\bar{\sigma}$. Thus if $|\bar{\sigma}/\tilde{q}| \geq O(1)$ (or less, if $R_r \gg L_r$), fluid element A is dragged to the right and B to the left (shown with broken arrows). The clockwise motion of $\tilde{\mathbf{v}}$ then pushes A downward and outward to the adjoining zone and B upward towards the annulus's boundary. If the sign of the shaded vortex were reversed so that it were prograde, then both $\bar{\mathbf{v}}$ and $\tilde{\mathbf{v}}$ initially move A to the right and B to the left. Then the counterclockwise $\tilde{\mathbf{v}}$ would pull both A and B away from the boundaries toward the center of the belt. Thus for $\bar{\sigma}/\tilde{q} = O(1)$, prograde $\tilde{q}$ is drawn in towards the center of a belt or zone while adverse $\tilde{q}$ is expelled.

6.2   Vortices with Uniform $\tilde{q}$

Two-dimensional vortices with uniform $\tilde{q}$ are frequently studied because they are completely specified by the locations of their one-dimensional boundaries, and the stable, steady (in frame U_x) solutions are uniquely determined by the values of $\tilde{q}$, the potential vortex area A, and the momentum P_x. The equilibria are exactly elliptical in shape for infinite L_r, $\bar{\mathbf{v}} = -\bar{\sigma}y\hat{\mathbf{x}}$, and constant $\bar{\sigma}$. They were first calculated by Moore & Saffman
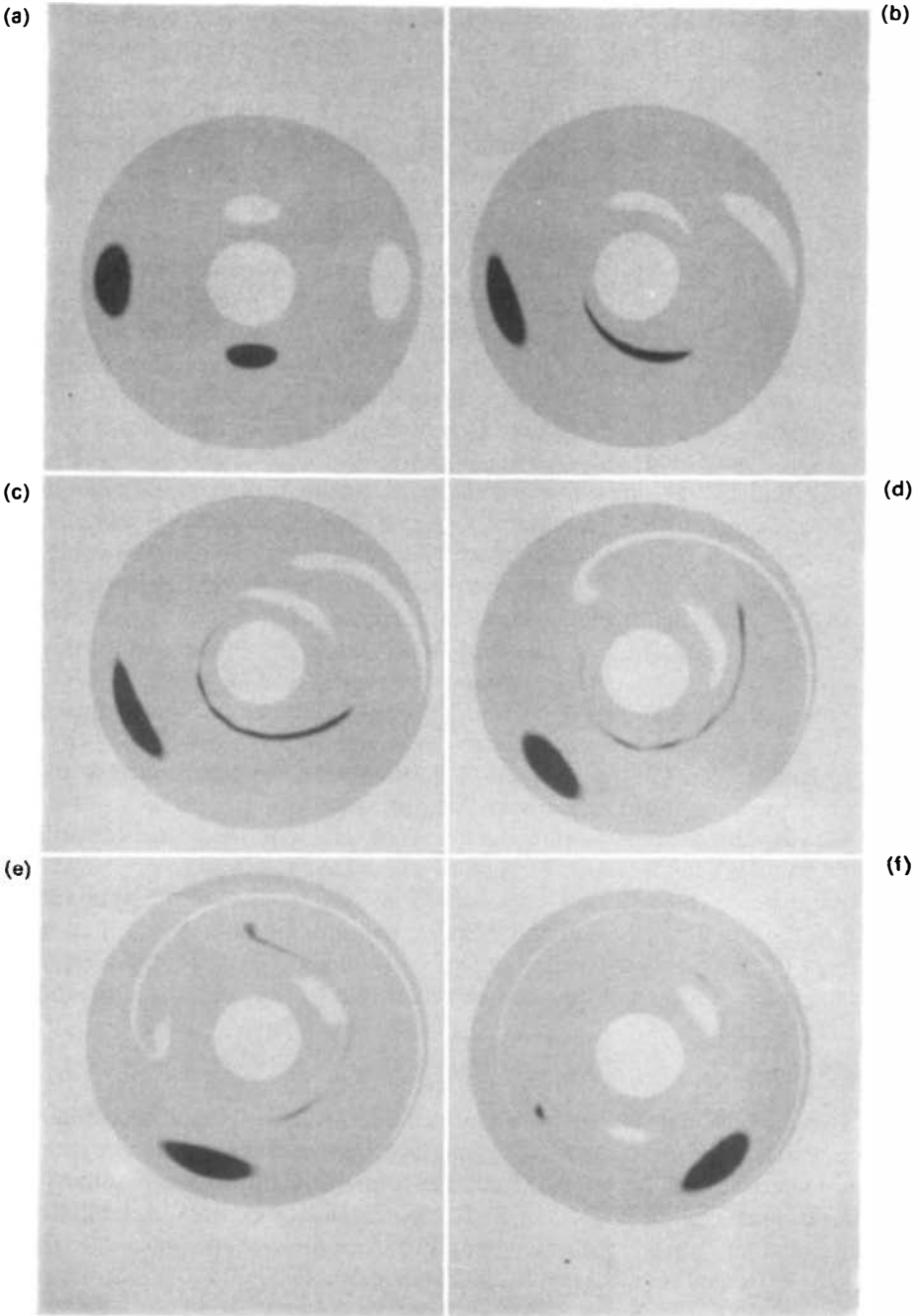
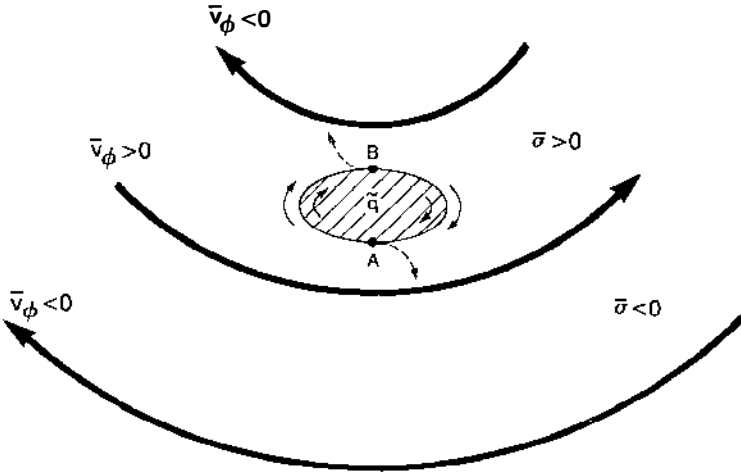*Figure 6* Schematic of Figure 5a showing how adverse $\tilde{q}$ is expelled. The dark, adverse, potential vortex with $\tilde{q} < 0$ is drawn shaded, and it lies in an adverse belt with $\bar{\sigma} > 0$. The $\bar{\mathbf{v}}(r)$ is represented by heavy arrows. See text for details.

(1971). For finite L_r or more general $\bar{\mathbf{v}}$, the shapes of the vortex boundaries are not known analytically and must be found numerically with contour dynamics (Overman & Zabusky 1982, Van Buskirk & Marcus 1993a). It is worthwhile to examine the dynamics of uniform-$\tilde{q}$ vortices because they occur commonly. The GRS has nearly uniform $\tilde{q}$ (Marcus 1988a, Dowling & Ingersoll 1989) as do vortices in numerical experiments (Marcus 1988b) that form from the chaotic merger of small vortices with different $\tilde{q}$ (a proposed scenario for the formation of Jovian vortices).

For the steady Moore-Saffman vortices the aspect ratio λ (maximum extent in longitude divided by extent in latitude) as a function of $\bar{\sigma}/\tilde{q}$ is

$$\lambda = \left(1 + \frac{\bar{\sigma}}{\tilde{q}}\right) M(\bar{\sigma}/\tilde{q}) \tag{24}$$

where

Figure 5   The evolution of four initially elliptical, infinite-L_r, potential vortices is an annulus embedded in $\bar{\sigma}(r) = r/3[(\bar{r}/r)^3 - 1]$ at six different times. The boundaries are $R_{in} = 1/3$ and $R_{out} = 4/3$. The $\bar{\sigma}(r)$ is negative for $r > \bar{r}$ and positive for $r < \bar{r}$, where $\bar{r} \equiv (R_{in} + R_{out})/2$. The light (dark) vortices have $\tilde{q} > 0$ ($\tilde{q} < 0$) and the gray has $\tilde{q} = 0$. Light vortices are prograde in the inner half and adverse in the outer half of the annulus. The pieces of vorticity that are initially adverse but cross over $r = \bar{r}$ to become prograde, develop tadpole-like heads and survive, while the pieces left behind continue to stretch and eventually decay. See text for details.

$$M(\chi) \equiv \frac{1+\chi \pm \sqrt{1+6\chi+\chi^2}}{2+2\chi}. \tag{25}$$

There are two solutions (one is linearly unstable) for adverse vortices but only one (corresponding to the positive square root in Equation 25) for prograde. Because $M(\chi) \simeq 1$ for $\chi > 0$, the λ of prograde vortices increases almost linearly with $(1+\bar{\sigma}/\tilde{q})$. There are no Moore-Saffman solutions for $\bar{\sigma}/\tilde{q} < (2\sqrt{2}-3) \simeq -0.17$. Adverse vortices are linearly or finite-amplitude unstable (see Section 8). For example, contour dynamics show that the boundaries of linearly stable vortices with uniform-$\tilde{q}$ embedded in adverse shear are unstable to the repeated shedding of very small, hair-like filaments. This type of filamentation was first observed in uniform-$\tilde{q}$ vortices with $\bar{\mathbf{v}} \equiv 0$ by Dritschel (1988). However, numerical calculations show that small-scale filamentation does not occur in prograde vortices with $\bar{\sigma}/\tilde{q} = O(1)$ (Van Buskirk & Marcus 1993b).

Stable vortices with nearly, but not exactly, uniform $\tilde{q}$ and vortices with finite L_r, or which are embedded in an annular $\bar{\mathbf{v}}(r)$ or in a $\bar{\mathbf{v}}$ with non-constant $\bar{\sigma}$ have many of the same properties as the Moore-Saffman vortices: They are steady or nearly steady in time; they have east-west (but not north-south) symmetry; and they are approximately elliptically shaped with λ increasing with $\bar{\sigma}/\tilde{q}$. For small values of $L_r/\sqrt{A}$ there are significant departures from the λ vs $\bar{\sigma}/\tilde{q}$ relation in Equation (24), and this is discussed in Section 9. Laboratory experiments show that prograde QG vortices are stable even when the surrounding fluid is very turbulent (Sommeria et al 1988).

A uniform-$\tilde{q}$ vortex as a model for the GRS was proposed by Marcus (1986, 1988a) who found that by using the measured ellipticity (2:1) and area of the GRS as constraints, a 1-parameter family of model vortices could be determined. For each value of $\tilde{q}/\bar{\sigma} \geq 1.5$ there is a value of L_r that satisfies the constraints. For example, $\tilde{q}/\bar{\sigma} = 1.5$ with an infinite L_r (a Moore-Saffman vortex) and $\tilde{q}/\bar{\sigma} = 15$ with $L_r = 2500$ km (the model in Figure 3) both satisfy the constraints but have very different velocities. The velocities of the Moore-Saffman vortex are not in good agreement with the observations. The "best" uniform-$\tilde{q}$ model can be found 1. if L_r is independently known, 2. a fit is made to the observed v (as done in Figure 3), or 3. $\tilde{q}$ is measured. (From Section 4, the value of $\tilde{q}$ is equal to the difference in the maximum and minimum values of ω on the inner and outer edges of the circumferential ring of velocity; it is not equal to the average value of $\tilde{\omega}$ in the GRS.) [Using the area and ellipticity of the GRS, Polvani et al (1990) modeled it with a non-oscillating Kida ellipse, apparently unaware that that solution is identical to the Moore-Saffman vortex, and therefore unaware that its velocities are not in good agreement

with the observations. They estimated $\tilde{q}$ by setting it equal to the average value of $\tilde{\omega}$ inside the GRS.]

Initial-value experiments of prograde vortices with nonuniform $\tilde{q}$ (and infinite L_r) show that they readjust their distribution of $|\tilde{q}|$ so that it decreases monotonically outward from the vortex center to the vortex edge. In many cases it can be shown that a prograde vortex with $|\tilde{q}|$ increasing outward from its center is linearly as well as finite-amplitude unstable. If the core is only slightly less rotational than the outer parts of the vortex, the $\tilde{q}$ in the core is pushed to the vortex edge, but if the $\tilde{q}$ of the core is more than $\sim 25\%$ weaker than the edge, the vortex violently breaks into pieces, many of which reassemble into a vortex with $|\tilde{q}|$ decreasing outward. With small L_r, a stable vortex can have $|\tilde{q}|$ increase slightly outward from its center.[5] In general, adverse vortices with nonuniform $\tilde{q}$ exist only for $0 > \bar{\sigma}/\tilde{q} \gg -1$ and are linearly or finite-amplitude unstable.

Moore-Saffman-like, steady, prograde potential vortices have been found to arise naturally in weakly dissipative numerical experiments with several types of initial conditions: 1. an initial patch of prograde $\tilde{q}$ adjusts its shape and distribution of $\tilde{q}$ until it relaxes to an approximately steady equilibrium, possibly with some pieces of $\tilde{q}$ so stretched by $\bar{v}$ that they detach from the core of the vortex decreasing its area; 2. a linearly unstable prograde vortex layer develops a linear Kelvin-Helmholtz instability with wavenumber m (Marcus 1986), forms m waves, and breaks into m separate vortices which then merge together into one large vortex (Figure 7); and 3. many small initial patches of prograde $\tilde{q}$ merge while the adverse patches disperse and decay. The second and third scenarios highlight the fact that prograde vortices tend to merge when their separation in latitude is less than the sum of their semi-minor axes. Mergers are discussed in detail in the next section. One surprise from these initial-value experiments is that at late time, prograde vortices are always approximately steady in time. Linearly stable, time-dependent vortices exist, such as the Kida (1981) ellipses whose axes oscillate, rotate, and stretch in time. But for $\bar{\sigma}/\tilde{q} = O(1)$,

---

[5] The critical gradient of $\tilde{q}$ for stability has been computed for only a few vortices. The best two-contour vortex fit to the GRS (i.e. two nested contours with $\tilde{q}_1$ inside the inner contour, $\tilde{q}_2$ between the contours, and zero elsewhere) is the one with the smallest possible value of $\tilde{q}_1$ such that the vortex is still stable (Figure 3). This figure suggests that Jovian vortices might have critical gradients of $\tilde{q}$. A scenario by which Jovian vortices could develop critical gradients is as follows: Dissipative vortices replenish their $\tilde{q}$ by accreting vortices with large $\tilde{q}$. (Vortices with small $\tilde{q}$ are passive, follow the streamlines around the GRS, never approach it, and so they cannot merge. Large $\tilde{q}$ vortices disrupt the streamlines so that they collide with the GRS's outer edge.) The GRS accumulates large $\tilde{q}$ on its boundary while its interior decays. Current calculations are testing whether the gradient of $\tilde{q}$ eventually exceeds its critical value causing an avalanche of high $\tilde{q}$ inwards, and whether the process is cyclic and keeps the gradient of $\tilde{q}$ near critical.

(a)

(b)

(c)

(d)

(e)

(f)
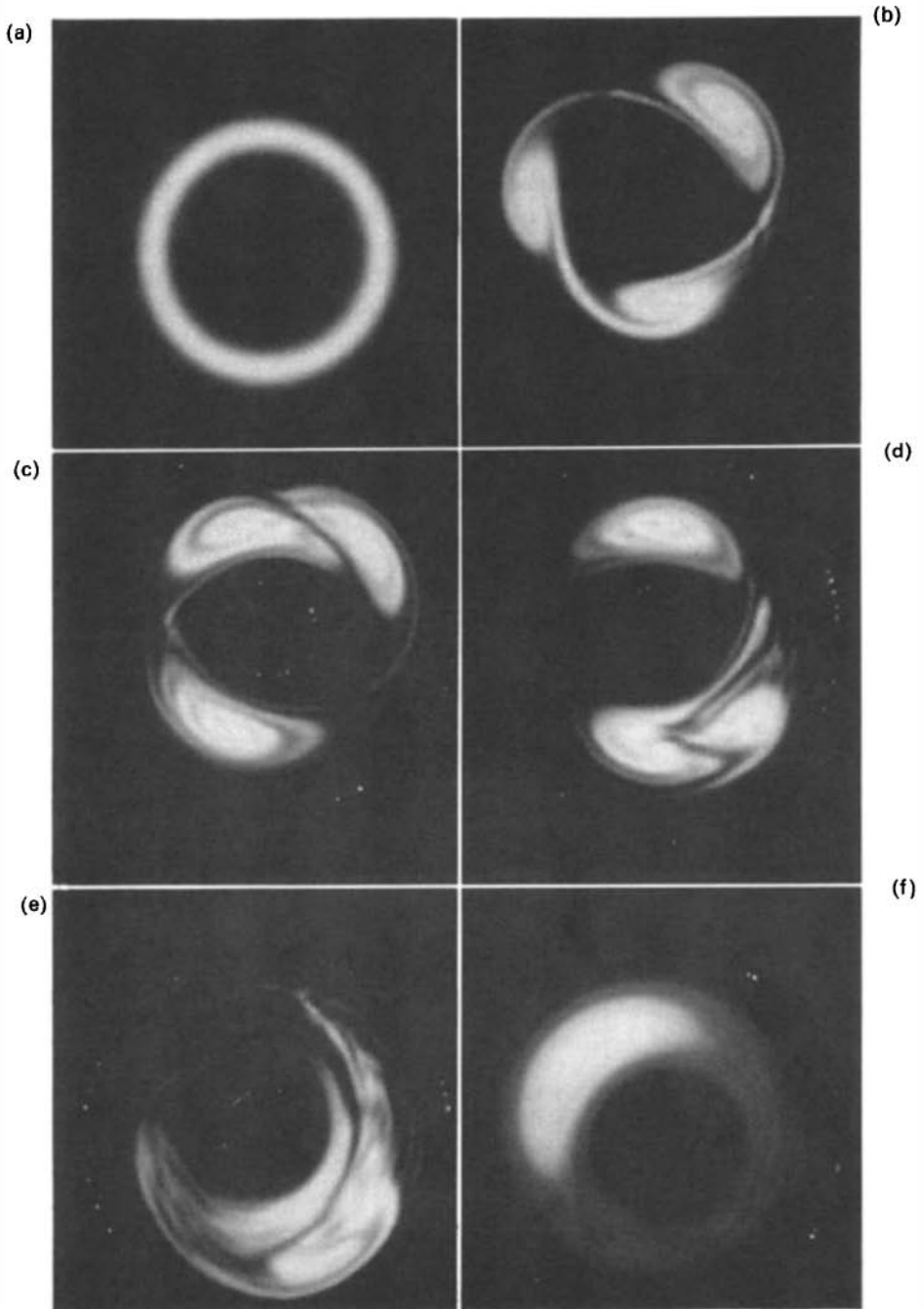
these solutions are unstable; the tips of the vortices shed $\tilde{q}$ which is then carried away from the vortex core by $\bar{v}$. The vortices readjust their sizes and shapes until their major axes align with the direction of $\bar{v}$. A vortex does not relax to an exactly steady state, but its residual oscillation is small, and its time-averaged distribution of $\tilde{q}$ is nearly equal to an exact, steady equilibrium (Van Buskirk & Marcus 1993b, Marcus & Van Buskirk 1993). Polvani et al (1990) proposed an oscillating Kida ellipse as a model of the Great Dark Spot of Neptune. They did not examine the finite-amplitude stability of their model nor did they examine how it might form from initial conditions. My own calculations (1990) suggest that it is unstable; moreover, I was not able to find plausible initial conditions from which it could form. This suggests that a new piece of physics is required.

The main conclusion from numerical experiments, is that prograde vortices with nearly uniform $\tilde{q}$, embedded in zone-belts with nearly uniform $\bar{\sigma}$, and with $\bar{\sigma}/\tilde{q} = O(1)$ relax to unique stable equilibria which are analogs of the steady Moore-Saffman vortices. The equilibria are completely determined by $\langle \bar{\sigma}/\tilde{q} \rangle$, A, L_r, and P_x.

It was first argued by Marcus (1988a) that if the Jovian weather layer is QG, then all of its vortices should be prograde. Prior to 1988, most theories of the GRS did not consider the zone-belt flow important, and if they included it at all, treated it as a hindrance to overcome or a small perturbation (Williams & Yamagata 1984). In support of QG theory, the *Voyager* images show that all of the Jovian vortices whose direction of rotation can be determined have their centers in prograde shear. In QG theory the planet's zone-belt flow is crucial for long-lived vortices: It not only expels adverse $\tilde{q}$ and attracts prograde $\tilde{q}$ but also by promoting the merger of prograde vortices makes them robust to large perturbations; if turbulence breaks them apart, the subsequent merger of the fragments makes them re-form. The tendency of prograde vortices to merge also provides (in a quantitative way—see the next section) an explanation for Ingersoll & Cuong's hypothesis (1981) that large Jovian vortices could be created by the merger of small ones [whose existence might be due to the $(q/H_0)(\partial v_z/\partial z)$ forcing from the local Jovian weather's vertical velocity].

However, a drawback of QG theory is that its cyclones and anti-cyclones behave similarly. Any asymmetry in their properties such as their relative

Figure 7 Evolution of a linearly unstable potential vortex layer embedded in prograde shear, $\bar{\sigma}(r) = r/3$, and in the same annular geometry used in Figure 5. Initially, $\bar{\sigma}(\bar{r})/\tilde{q}(\bar{r}) = 0.28$. Flow with $\tilde{q} > 0$ is light and with $\tilde{q} = 0$ is black. The layer breaks into a 3-fold symmetric eigenmode (the most rapidly growing for this geometry). The three vortices separate from each other, merge together, and eject the nearly irrotational fluid entrained near the vortex center. Reproduced by permission from Marcus (1986).

numbers must be attributable to the asymmetry of the zones and belts in which they lie. So if one assumes a priori that the belts and zones are similar, QG theory predicts approximately equal numbers of cyclones and anti-cyclones. By contrast, most non-QG cyclones and anti-cyclones act differently. Williams & Yamagata (1984) showed that IG cyclones are much more unstable and less likely to form than IG anti-cyclones, and argued that Jovian vortices should be anti-cyclonic in agreement with Mac Low & Ingersoll (1986) who reported that 90% of their observed Jovian vortices were anti-cyclones. However, most of the observed anti-cyclones were small with $R_x < 1300$ km $\leq L_r$, and Williams (1985) has argued that the small Jovian vortices with $R_x \leq L_r$ should be QG not IG. Thus the preponderance of small Jovian anti-cyclones is puzzling. One possible explanation is that the upwelling convective plumes that produce the small anti-cyclones (which feed the large, observable anti-cyclones) are much more concentrated and intense than the downward flow which produces cyclones. Another explanation is that cyclones may be easily overlooked in the *Voyager* images because their clouds are often diffuse and fila-mentary while those of the anti-cyclones are bright and compact (see the next section).[6]

6.3   Cloud Morphologies

In QG theory, Jovian cyclones and anti-cyclones behave the same; yet, in many cases their associated cloud patterns are different. Anti-cyclones have smooth, nearly elliptical clouds, while cyclones (except for those at 14°N, which are unusual) have large, filamentary, diffuse cloud patterns twisted in all directions (Figure 4). Based on these patterns M. V. Nezlin (1991, private communication) argued that cyclones could not be long-lived and were dynamically different from anti-cyclones because their velocities were disorganized. Here is an alternative explanation that shows that the clouds and ψ are not necessarily aligned. Dissipative vortices often create a weak Ekman circulation: in the upper half of a Jovian vortex there is upwelling where $\tilde{\omega}/f(y) < 0$ and downwelling where $\tilde{\omega}/f(y) > 0$ (Flaser et al 1981). The rising (sinking) motions in the sub-adiabatic top of the weather layer cool (heat) the upper vortex. The vertical velocities would be too small to be detectable, but the *Voyager* infrared measurements confirm that the anti-cyclonic center of the GRS is cooler than its sur-roundings and that the centers of the cyclonic barges are warm (Hanel et al 1979). Assuming that the visible condensate in the clouds advects with the horizontal velocity and that it is created randomly where the flow is cooled

---

[6] Mac Low & Ingersoll (1986) used images in the violet and UV bands. It is possible that the warmer clouds of cyclones may be more visible at other wavelengths.

and destroyed where it is warmed, Marcus & Graves (1993) randomly created small cloudlets of passive tracers in a numerical simulation of Jovian vortices at locations where $\tilde{\omega}/f(y) < 0$ (i.e. interior to, especially along the vortex boundary of, the anti-cyclones and just outside the vortex boundary of the cyclones), and randomly destroyed them where $\tilde{\omega}/f(y) > 0$ (i.e. inside the cyclones and just outside the anti-cyclones). The velocities of the cyclones and anti-cyclones were identical in their simulations and consisted of a steady-state equilibrium vortex plus weak, time-dependent, small-scale turbulence. The cloud patterns of the cyclones and anti-cyclones looked very different. Tracers filled the interiors of the anti-cyclones where the differential rotation and turbulence homogenized them. Tracers pushed outside the anti-cyclones were destroyed and left a circumferential ring with a tracer density lower than the ambient background like the dark rings around the anti-cyclones in Figure 4 at 41°S. Cloudlets created outside cyclones were repeatedly sheared by **v** and twisted by the turbulence. These tracers never homogenized. Like the clouds of the cyclones at 41°S in Figure 4, their contours of constant tracer density (brightness) were filamentary, diffuse, and not aligned with the mean ψ.

7. VORTEX MERGER

We present a heuristic explanation for prograde vortex merger. We assume that the length over which $\bar{\sigma}$ varies is large compared to $\sqrt{A}$ so that $\bar{\mathbf{v}}(y)$ can be approximated by a Taylor series expansion, $\bar{v}_x(y) \simeq -\sigma_0 y$, where σ_0 is constant; the origin is the center of potential vorticity, and we are in a moving frame so $\mathbf{U} = \mathbf{0}$. Consider two prograde vortices embedded in this $\bar{\mathbf{v}}$ so that they are in quasi-equilibrium in the sense that if they were infinitely far apart they would be exact, steady equilibria with their major axes in the x direction. For simplicity let both vortices have the same A and $\tilde{q}$, and let the centers of the two vortices be at $(x, y) = (\pm D/2, \pm b/2)$. The differential velocity in $\bar{\mathbf{v}}$ will push the two vortices together in x (even if initially $b = 0$, $\tilde{v}_y$ would quickly make it non-zero). If the two vortices merge, we can predict a great deal about the merged vortex: 1. its value of $\tilde{q}$ is the same as the initial two vortices because Equation (8) conserves $\tilde{q}$ (though see below); 2. it is a steady vortex with its major axis in the x direction because that is the only robust solution; 3. the center of its potential vorticity is the origin because P_x is conserved and because $U_x = 0$; 4. its area is equal to $2A$ because circulation is conserved by Equation (11) (though see below); and 5. the λ of the merged vortex is known because it is a function of $\bar{\sigma}/\tilde{q}$ (both the numerator and denominator are conserved in the merger) and of $\sqrt{A}/L_r$ (for infinite L_r, the λ of the final and initial vortices are the same). The energy of the initial two vortices and final

merged vortex will differ, and the usual energy argument used in fluid dynamics states that a flow will undergo a kinematically allowable transition if the energy of the final state is less than the initial. The change in self-energy ΔE_{self} is given by (14). For infinite L_r and to leading order in R_y/D, it is

$$\Delta E_{self} = \frac{\tilde{\Gamma}^2}{2\pi}\left[\frac{1}{4} + \ln\frac{D}{R_y(1+\lambda)} + O\left(\frac{R_y}{D}\right)\right] > 0, \tag{26}$$

where R_y is the minor radius. For finite L_r, ΔE_{self} must be computed numerically and is generally much less than Equation (26), but it always increases in a merger between two vortices with the same sign of $\tilde{q}$. It does so for the same reason and in quantitatively the same way as the self-energy increases when two, two-dimensional patches of electric charge with the same sign and finite Debye length are brought together. Thus ΔE_{self}, which is the same for prograde or adverse vortex merger, always increases and inhibits the merger. From Equation (16) the change in the interaction energy is

$$\Delta E_{int} = -\Delta\left(\frac{\sigma_0 \tilde{q}}{2}\int y^2\, d^2r\right). \tag{27}$$

For finite-L_r vortices, the integral in (27) must be computed numerically over the domains of the vortices, but for infinite L_r:

$$\Delta E_{int} = -\frac{\tilde{\Gamma}^2 \sigma_0}{4\pi\lambda\tilde{q}}\left(1 - \frac{b^2}{R_y^2}\right). \tag{28}$$

In all cases, the sign of ΔE_{int} depends upon the sign of $\sigma_0/\tilde{q}$. For small b, prograde (adverse) vortex merger decreases (increases) E_{int}. Thus while ΔE_{self} inhibits merger, ΔE_{int} aids prograde vortex merger and inhibits adverse vortex merger (for small b). It must be noted that there can be two important modifications to the above scenario. One is that as vortices merge they often entrap irrotational fluid. At late times the rotational and irrotational fluid become well mixed (Van Buskirk & Marcus 1993b), so that the effective $|\tilde{q}|$ of the merged vortex is less than that of the original, and its effective area is greater than $2A$. Another is that often some of the initial $\tilde{q}$ is stripped away from the merging vortices (generally leaving it at values of y greater than R_y) making the final area smaller than $2A$. Both effects decrease ΔE_{self} because less $\tilde{q}$ is brought close together, and for prograde (adverse) vortices both effects decrease (increase) ΔE_{int} because both increase $\Delta(|\int y^2\, d^2r|)$. Thus these effects reduce the inhibition to merge caused by E_{self} and accentuate the differences in ΔE_{int} between prograde

and adverse vortices. In numerical experiments with small L_r and for mergers between vortices with unequal areas (the case for Jovian vortices), the entrainment of irrotational flow and the stripping of $\tilde{q}$ are less. As b increases, ΔE_{int} increases for prograde vortices (cf Equation 28). There exists a critical value b_{crit} such that for $b > b_{crit}$, the total change in energy ($\Delta E_{self} + \Delta E_{int}$) would increase in a merger. Numerical experiments have confirmed to within 5% that prograde vortices with $b < b_{crit}$ merge, and those with greater values do not (Marcus 1990). Generally, b_{crit} is approximately equal to the sum of the semi-diameters in the y direction of the merging vortices.

Two adverse vortices with large b could in principle lower their energy by merging, but clearly it is necessary for the vortices to approach each other before they could merge. Because the vortices move with $\mathbf{v}$, it is not obvious how they could do so and overcome their large initial separation in b. Therefore, it is not surprising that we know of no numerical or observational examples of adverse vortex merger with $|\bar{\sigma}/\tilde{q}| > 0.1$. In fact, it is energetically favorable for a single adverse vortex to fission (leaving the broken pieces at the latitude of the initial vortex) which explains, in part, their finite-amplitude instability.

When $\bar{\mathbf{v}} \equiv \mathbf{0}$ (which makes $\Delta E_{int} \equiv 0$) merger is not impossible, but it is more difficult. For these vortices to merge they must be initially very close because there is no differential velocity in $\bar{\mathbf{v}}$ to push them together (Overman & Zabusky 1982). Furthermore if there are no boundaries, angular momentum about the center of potential vorticity (and every other point) is conserved so the movements of the vortices are very constrained. Merging vortices with $\bar{\mathbf{v}} = \mathbf{0}$ conserve their energy and angular momentum by shooting filaments of $\tilde{q}$ far away from the merging vortices creating a halo around the merged core. Thus the area of the core is always less than $2A$, and the mergers are qualitatively different from those with $\bar{\sigma}/\tilde{q} = O(1)$.

8.   VORTEX SIZE

For infinite L_r and constant $\bar{\sigma}$, QG vortices have no characteristic size because Equation (8) is invariant under changes in scale s: If a vortex with $\tilde{q}(x, y, t)$ is a solution, then so is a vortex s times larger with $\tilde{q}(sx, sy, t)$. Spatial variations in $\bar{\sigma}$ or finite L_r break this invariance. Clearly, $\bar{\mathbf{v}}$ can limit the size of a vortex. Consider a Jovian vortex in a prograde zone sandwiched between two adverse belts. If the vortex were to grow in size by merging with smaller vortices it could eventually overflow its zone into the surrounding belts. Because the belts tend to expel the (locally) adverse $\tilde{q}$, the vortex overflows only a finite extent and is thereby limited in size.

This section shows how $\bar{\mathbf{v}}(y)$ sets the size of vortices in flows with infinite L_r, and the next section shows how finite L_r changes these results.

A potential vortex embedded in a $\bar{\mathbf{v}}$ that is everywhere prograde has only closed streamlines around it, but the vortex in Figure 8 has both open and closed streamlines. The $\bar{\sigma}(y)$ south of $y = Y_{\bar{\sigma}}$ (*dotted line*) is prograde, and north of it the $\bar{\sigma}(y)$ is adverse, i.e. $y = Y_{\bar{\sigma}}$ is a zone-belt boundary with $\bar{\sigma}(Y_{\bar{\sigma}}) = 0$. The center of the vortex lies in prograde shear. Moving north from $Y_{\bar{\sigma}}$, one crosses the latitude where $\bar{\mathbf{v}} = 0$ (*dashed line*), and then reaches the stagnation point where $\mathbf{v} = 0$ (and streamlines cross). If the vortex is steady, then the streamlines are closed in its immediate vicinity, but there is a last closed streamline (LCS) that passes through the stagnation point. In an unbounded flow the streamlines exterior to the LCS are open. The boundary of the vortex which is itself a streamline could lie anywhere between the vortex center and the stagnation point without qualitatively changing Figure 8.

Much of the dynamics that occurs in a zone-belt flow like Figure 8 can be illustrated with uniform-$\tilde{q}$ vortices embedded in a quadratic $\bar{\mathbf{v}}$. The unit of time is chosen so that $\tilde{q} = 1$, and of length so that

$$\bar{v}_x(y) = -\sigma_0 y + y^2/2 + c. \tag{29}$$

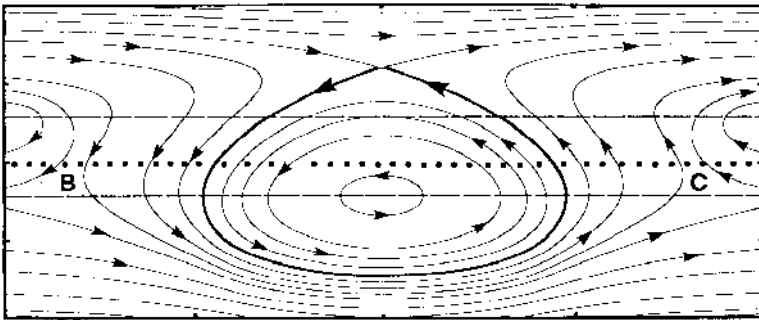(The constant c is unimportant by Galilean invariance and is chosen to

Figure 8   Schematic of the steady streamlines of a $\tilde{q} > 0$ potential vortex embedded in a $\bar{\mathbf{v}}(y)$ that is prograde south of $Y_{\bar{\sigma}}$ (*dotted line* where $\bar{\sigma} = 0$) and adverse to the north. There are two latitudes where $\bar{\mathbf{v}} = 0$ (*dashed lines*). The last closed streamline (*heavy line*) crosses itself at the stagnation point. If these were the streamlines of a time-averaged Jovian flow, then finding the stagnation point by locating where the paths of small tracer clouds diverge from each other is unreliable. Turbulence in the lee of the vortex could easily push a tracer from one time-averaged streamline to another leaving the impression that locations like **B** and **C** are stagnation points.

make $U_x \equiv 0$.) Figure 9 shows the boundaries of eight, steady-state poten-
tial vortices embedded in the $\bar{v}$ of Equation (29) with $\sigma_o = 1$. Each vortex
has its center at the origin (i.e. $P_x = 0$) and has an infinite L_r, but each
vortex has a different area A. The smallest is nearly an elliptical Moore-
Saffman vortex, but the larger ones which extend into the region of adverse
shear north of $y = 1$ are distorted on their northern boundaries. The
largest vortex in Figure 9 completely fills the region inside its LCS. Its
boundary touches the stagnation point which produces a corner at its
northernmost point. It is the *limiting vortex*, and it is the end of this family
of vortices. (It is not a turning point of the family. See Section 9.) Clearly,
a steady vortex cannot be larger than its own LCS as it would have its
extremities outside the LCS carried away along the open streamlines. The
vortices in Figure 9 are linearly stable, but they (and all vortices with an
LCS, including the adverse Moore-Saffman vortices) are finite-amplitude
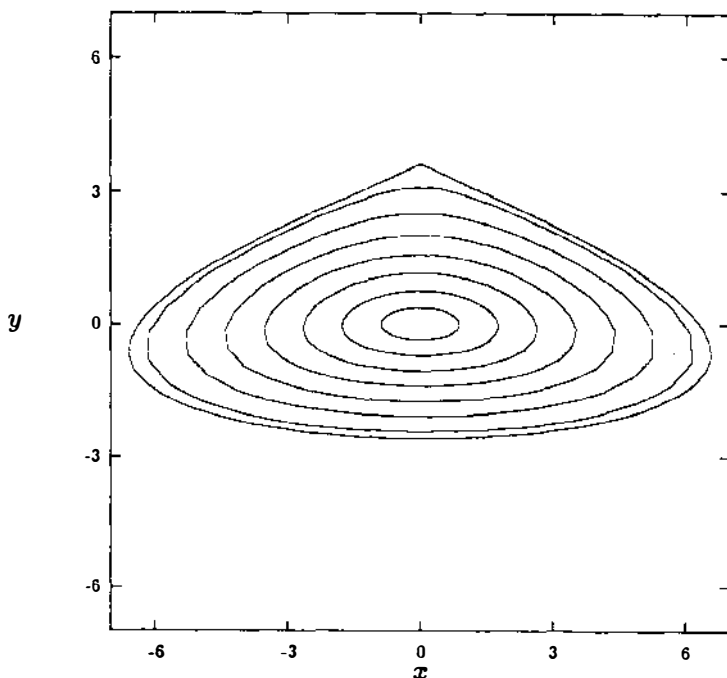

Figure 9   Boundaries of eight different infinite-L_r, potential vortices all with $\sigma_\bullet = 1$ embedded
in the $\bar{v}_x(y)$ of Equation (29) and different values of A. The largest vortex with $A = 55.135$
is the limiting solution and has a stagnation point on its boundary. The shear is adverse for
$y > 1$.

unstable. Numerical experiments show that the minimum distance between the LCS and the vortex boundary is a good measure of how large a perturbation is needed to disrupt the vortex (Marcus 1990). All of the vortices in Figure 9 have streamlines that look qualitatively like those in Figure 8.

All Jovian vortices have centers that lie in a prograde shear, but they are usually sandwiched between two adverse belts or zones and have stagnation points on both their northern and southern sides. They can be understood by examining the dynamics of vortices embedded in a cubic $\bar{v}(y)$ flow. We choose the unit of time so that $\tilde{q} = 1$, and we choose the origin and unit of length so that:

$$\bar{v}_x(y) = -\sigma_o y + y^3/3 + c. \tag{30}$$

(The constant c is irrelevant due to Galilean invariance.) Consider the cubic $\bar{v}$ with $\sigma_o = 1$ and the family of uniform-$\tilde{q}$ potential vortices centered at the origin (i.e. $P_x = 0$, and the vortices are north-south symmetric) and with infinite L_r. The family is illustrated with the heavy curve in Figure 10
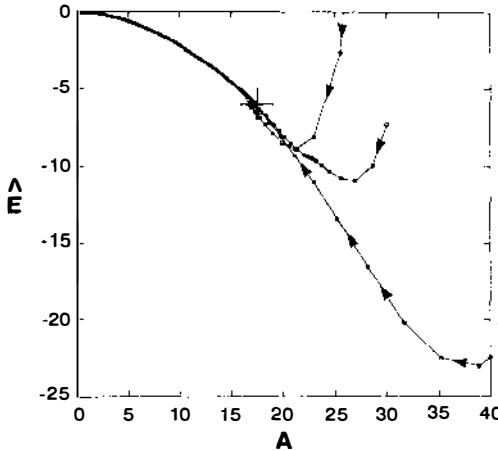

Figure 10   Reduced energy $\hat{E}$ as a function of area A. The heavy line from the origin to the $+$ shows the relation between $\hat{E}$ and A of the family of steady, stable, infinite-L_r, potential vortices with $P_x = 0$, and $\sigma_0 = 1$ embedded in the cubic $\bar{v}$ of Equation (30). The family ends with the limiting vortex at the $+$ (which is not a turning point). The limiting vortex has a stagnation point on its boundary. The evolutionary paths of three different initial vortices are shown as thin curves superposed with open circles. The dissipation monotonically decreases A in time, but conserves the initial values of $\tilde{q}$. The energy is not conserved. All of the paths are attracted to the plus sign; their slopes $d\hat{E}/dA$ there are approximately equal to the slope of the heavy curve at its limiting point.

which shows the reduced energy $\hat{E}$ as a function of A for the steady-state vortices in the family. [$\hat{E}$ is the total energy of the vortex given by the sum of Equation (14) and (16) minus a constant equal to the total energy of a non-equilibrium vortex with the same A and P_x, but exactly circular in shape.] If a small vortex in this family slowly increases its area A by merging with infinitesimally small vortices with $P_x = 0$, its evolutionary path in the $\hat{E}$-A plane follows the heavy curve in Figure 10 from the origin to the $+$ where the heavy curve ends. The $+$ corresponds to the limiting vortex with stagnation points on its most northern and southern boundaries. Any additional area added to the vortex leaks through the LCS at the stagnation points and is carried to infinity.

Also shown in Figure 10 are thin lines which represent the evolutionary tracks in the $\hat{E}$-A plane of three infinite-L_r, north-south-symmetric vortices that are initially far from equilibrium, embedded in the cubic $\bar{v}$ with $\sigma_0 = 1$, and governed by the QG Equation (8) with a small amount of dissipation added. The vortices move along the tracks from right to left (always decreasing their A) and are all attracted to the limiting vortex near the $+$. These evolutionary paths are representative of several dozen that we have computed in which the initial A was greater than that of the limiting vortex. All of the vortices arrive at the $+$ in Figure 10 in finite time, settle into nearly steady states that are very close to the limiting vortex, and at late times have slopes $d\hat{E}/dA$ approximately equal to the slope of the heavy curve at the limiting vortex. Obviously, an explanation is required of why the limiting vortex is such a robust attractor.

To understand Figure 10 consider the non-dissipative solution to Equation (8). Although the vortex boundary changes shape in time, conservation of energy and potential circulation $\tilde{\Gamma}$ keeps its location in the $(\hat{E}$-$A)$ plane fixed. The early evolution of an initially circular, infinite-L_r vortex with $P_x = 0$, $A = 30$, and embedded in the cubic $\bar{v}$ of Equation (30) with $\sigma_0 = 1$ is shown in Figures 11a,b. The $\bar{\sigma}$ is adverse for $|y| > 1$, and the northern and southern extremities of the vortex lie outside the initial LCS. The $\bar{v}$ quickly stretches the extremities into two thin tails and advects them towards $\pm \infty$. The flow never settles into a steady state. When dissipation—viscosity, Ekman pumping, etc—is added to the equations, the tails are most affected. They are carried away from the main body of the vortex by $\bar{v}$ and eventually decay. Numerical simulations show that the dynamics of the main body of the vortex (i.e. the part not in the thin tails) is insensitive to the exact form of dissipation. (Presumably, because the dissipation acts only at distances far from the main body of the vortex.) Because of this insensitivity, we put a model dissipation into Equation (8) when we compute the flows in Figures 10 and 11c,d: Any part of a vortex tail that extends past $|x| = X_{cut}$ is cut off from the main body of the vortex,
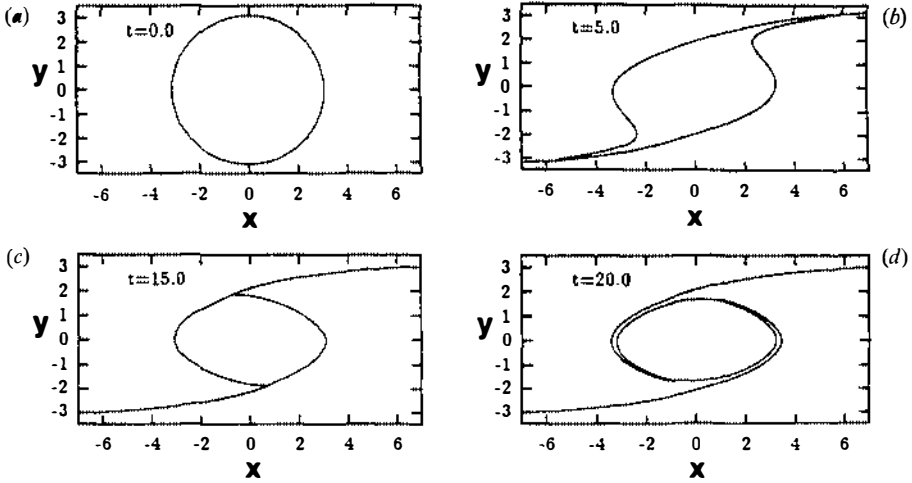
(a)

(b)

(c)

(d)

Figure 11   The evolution of the boundary of an initially circular vortex embedded in the cubic $\bar{v}$ of Equation (30) [corresponding to the middle evolutionary path in Figure 10 with initial $A = 30$] at four times. Figures *a* and *b* are computed with no dissipation, but *c* and *d* have the dissipation described in Section 8. For $|y| > 1$, $\bar{\sigma}$ is adverse.

and its $\tilde{q}(x, y, t)$ is set to zero. For the flows in Figures 10 and 11, we set $X_{cut} = 9.5$. All of the flows that are illustrated are stable to north-south asymmetric perturbations, so as the vortices evolve, any section of tail that is removed at positive y, has a corresponding piece removed at negative y. Thus P_x remains zero throughout the evolution.

This model dissipation conserves the value $\tilde{q}$ and P_x, but decreases the area A monotonically. (Note that $\tilde{q} = 1$, $\tilde{\Gamma} = A$.) Thus the tracks in Figure 10 all go from right to left. The $\hat{E}$ can increase or decrease with this dissipation. Figure 11 shows the evolution·of the vortex boundary corresponding to the middle evolutionary track in Figure 10. As with the dissipationless equations, the northern and southern extremities of the vortex are initially stretched by $\bar{v}$ into tails. Most of the potential circulation outside the last closed streamline is quickly carried far from the main body of the vortex and removed. (See Van Buskirk & Marcus 1993b for details of this evolution.) The boundary of the main vortex becomes nearly steady in time. Once the vortex has shed enough potential circulation so that its main body lies entirely within its last closed streamline, it stops evolving: No $\tilde{q}$ from the main body can cross the LCS, so no significant amount of it can reach $x = \pm X_{cut}$; the dissipation stops, and the flow stops moving in the $(\hat{E} - A)$ plane. Because the main body of the vortex stops evolving

just after it shrinks inside its LCS, it is nearly the same as the limiting vortex. Thus, all of the evolutionary paths in Figure 10 are attracted to the limiting vortex at the $+$.

In Figure 11 the two locations where the tails join onto the main vortex rotate counterclockwise around the main vortex indefinitely. However, the amount of potential circulation in the tails decreases exponentially in time, so the velocity is nearly steady. At late times, each vortex tail exterior to the LCS becomes coincident with one of the steady streamlines that connects a stagnation point to $x = \pm X_{\text{cut}}$. (In Figures 11c,d, the stagnation points are at the intersections of the y-axis and the two vortex tails.) This streamline is a stable attractor for the vortex tail. A consequence of this attraction is that the value of the stream function where the tail is cut ψ_{cut} approaches the value of ψ at the stagnation point ψ_{stag}. This fact explains why all of the paths in Figure 10 end with the same slope as the family of steady vortices: When an infinitesimal piece of potential vorticity of strength $d\tilde{\Gamma} = \tilde{q}\,dA$ is removed at position $\mathbf{x}$ from a vortex with potential circulation $\tilde{\Gamma}$ embedded in $\bar{\mathbf{v}}$ with a total stream function ψ, then the change in the total energy is

$$dE = -\psi(\mathbf{x})\,d\tilde{\Gamma}. \tag{31}$$

Equation (31) is the same expression for the energy change when an infinitesimal piece of electric charge of strength $d\tilde{\Gamma} = \tilde{q}\,dA$ is removed from a charge $\tilde{\Gamma}$ in an external electric field with total potential ψ. Using Equation (31) and our definition of $\hat{E}$,

$$d\hat{E} = -\tilde{q}\psi(\mathbf{x})\,dA + \frac{\tilde{q}\tilde{\Gamma}}{4\pi}\ln\left(\frac{\tilde{\Gamma}}{\pi}\right)dA. \tag{32}$$

As stated previously, if a vortex were to slowly grow by merging with other vortices, it would evolve along the heavy curve in Figure 10 from the origin to the $+$. It has been shown that when a vortex grows this way, all of the change in shape of the boundary at the end of the evolution occurs at the stagnation point (Van Buskirk & Marcus 1993b). Therefore, the slope $d\hat{E}/dA$ of the heavy curve in Figure 10 at the limiting vortex is

$$-\tilde{q}\psi_{\text{stag}} + \frac{\tilde{q}\tilde{\Gamma}_{\text{lim}}}{4\pi}\ln\left(\frac{\tilde{\Gamma}_{\text{lim}}}{\pi}\right), \tag{33}$$

where $\tilde{\Gamma}_{\text{lim}}$ is the value of $\tilde{\Gamma}$ of the limiting vortex. From (32) the slopes of the three evolutionary tracks in Figure 10 at any instant are

$$\frac{d\hat{E}}{dA} = -\tilde{q}\psi_{\text{cut}}(t) + \frac{\tilde{q}\tilde{\Gamma}(t)}{4\pi}\ln\left(\frac{\tilde{\Gamma}(t)}{\pi}\right). \tag{34}$$

We have shown that at late times $\psi_{\text{cut}} \to \psi_{\text{stag}}$ and $\tilde{\Gamma}(t) \to \tilde{\Gamma}_{\text{lim}}$. Therefore, Equations (33) and (34) show the slopes $d\hat{E}/dA$ of the evolutionary tracks at late times approach the slope of the family of solutions at the limit point.

This model dissipation shows that for infinite L_r, a vortex with initially large areas evolves to a limiting vortex. It also shows that an initially small vortex that slowly grows in size by merging with infinitesimal area vortices also evolves to the limiting vortex. However, most Jovian vortices that overflow into adverse regions of $\bar{v}$ are close to, but not equal to, a limiting vortex. We now show how the effects of finite L_r accounts for this discrepancy.

9.   FINITE L_r: SMALLER OVERFLOWS

Finite-L_r prograde vortices do not overflow into regions of adverse $\bar{\sigma}$ as far as their infinite-L_r counterparts. There are two reasons. One is that some families of vortices become linearly unstable before reaching their limiting solutions—we call these families *corner-like*. The other is that some families of prograde vortices never even reach the region of adverse shear—we call these families *band-like*.

The linear instability in corner-like families is readily observed in any bifurcation curve, such as the $\hat{E}$ vs A curve, as a saddle-node or turning point. The turning points for $L_r = 0.192$ and $L_r = 0.385$ are illustrated in Figure 12 which shows $\lambda(A)$ for families of prograde vortices with $P_x = 0$ embedded in the cubic $\bar{v}(y)$ of Equation (30) with $\sigma_o = 0.0833$. (The units and origin are the same as in Section 8.) The upper parts of the curves are linearly stable, and the bottom parts, containing the limiting vortices, are not. The turning and limiting points become nearly coincident in the family as $L_r \to \infty$. We call these families corner-like because they end with limiting vortices that have corners (stagnation points) on their boundaries. The two families with $L_r < 0.177$ are band-like.

A vortex with $L_r = 0.385$ and infinitesimal area that gradually increases A by merging with small vortices (centered at $y = 0$ to keep $P_x = 0$) evolves through a sequence of quasi-stationary equilibria along the curve of corner-like vortices in Figure 12 until it reaches its turning point. Then, its northern and southernmost boundaries waver—a symptom of the linear instability. Any additional accumulated area leaks out of these wavering tips, joins onto the open streamlines coming from the stagnation points, and is carried away (similar to the flow in Figure 11). Thus for values of
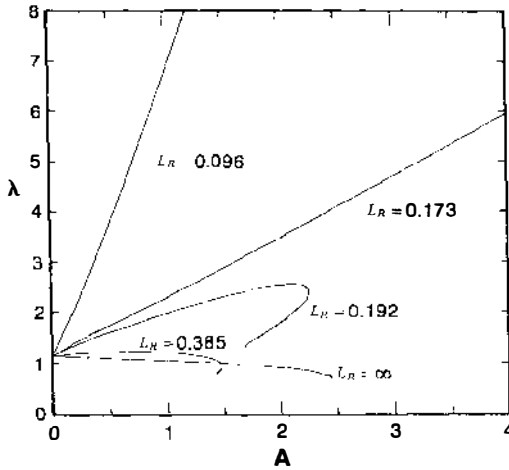
Figure 12 The aspect ratio λ (maximum length divided by maximum height) as a function of area A for 5 families of vortices embedded in the cubic $\bar{v}$ of Equation (30) with $P_x = 0$ and $\sigma_0 = 0.0833$. The asymptotically computed value of L_r^* from Equation (35) is 0.177. The two families with $L_r < L_r^*$ are band-like and can increase their areas indefinitely though they are bounded in longitude. The other families are corner-like, and their limit points correspond to vortices with stagnation points (corners) on their boundaries. The turning points, where the families become linearly unstable, approach the limit points as $L_r \to \infty$.

L_r where the families are corner-like vortices are attracted to turning points. They do not fill their LCSs, are east-west symmetric, have stagnation points just to their north or south (or both) but not on their boundaries which are smooth, and do not have corners like the infinite-L_r attracting vortices.

Prograde vortices with large σ_0 and small L_r embedded in the cubic $\bar{v}(y)$ of Equation (30) are members of band-like families. As Figure 12 shows, for each value of P_x and σ_0 there is a critical value L_r^* such that families of vortices with $L_r > L_r^*$ have limiting solutions and are corner-like and those with $L_r < L_r^*$ do not and are band-like. For band-like vortices the shear and the screening effects of L_r are too strong for the vortices to have much influence on the $\tilde{q}$ at their northern and southernmost extremities. Therefore they are stretched in the x direction by $\bar{v}$. Thus, as a band-like vortex increases its A, the additional area is not added equally to all parts of the vortex but preferentially to its eastern and western ends. As A increases, the vortex goes from an ellipse [with λ as a function of $\bar{\sigma}/\tilde{q}$ given by equation (24)] to a flatter more eccentric shape. Asymptotically the growth on the northern and southern sides stops while the vortex continues to expand in longitude. The family of vortices asymptotes to an east-west

band of $\tilde{q}$ with infinite area extending to $x = \pm\infty$ and filling all space between two finite, bounding latitudes at $\pm Y_{max}$. Thus band-like vortices grow flatter as A increases, so they never reach the region of adverse $\bar{\sigma}$. They are linearly stable (with no turning points in the family) and have no analog for $L_r \to \infty$. For $P_x = 0$ (i.e. for vortices centered in the cubic zone-belt flow), $L_r^*(\sigma_0)$ has been computed numerically and is in good agreement with an analytically-obtained approximation derived by Marcus & Van Buskirk (1993) using an asymptotic expansion in small L_r (Pratt & Stern 1986). For $P_x = 0$ this approximation in our dimensionless units is

$$L_r^* = 2(0.12)^{1/6}\sigma_0^{5/6} \simeq 1.4\sigma_0^{5/6}. \tag{35}$$

The latitudes where the cubic $\bar{v}$ in equation (30) has $\bar{\sigma} = 0$ are $y \equiv \pm Y_{\bar{\sigma}} = \pm\sqrt{\sigma_0}$, so in dimensional units $L_r^*/Y_{\bar{\sigma}} = 1.4[\bar{\sigma}(0)/\tilde{q}]^{1/3}$.

The change in shape with A of a band-like family of vortices is illustrated in Figure 13 for $\bar{\sigma}/\tilde{q} = 0.5$, $P_x = 0$, and finite L_r. Here, the vortices are embedded in the simpler Moore-Saffman zone-belt: $\bar{v}_x = -\sigma_0 y$ to emphasize the fact that the band-like shape and lack of limiting solution are not consequences of the cubic $\bar{v}(y)$, but are general properties of prograde vortices with large $\sqrt{A}/L_r$. For infinite L_r, all of the Moore-Saffman vortices with $\bar{\sigma}/\tilde{q} = 0.5$, regardless of their values of P_x or A, have the same shape (though, different size). All families of finite-L_r vortices embedded in $\bar{v}_x = -\sigma_0 y$ are band-like. A vortex with infinitesimal A has the same shape as the Moore-Saffman vortex, but as Figure 13 shows, its aspect ratio λ increases with $\sqrt{A}/L_r$. For $\bar{v}_x = -\sigma_0 y$, the maximum latitudes $\pm Y_{max}$ to which a family of finite-L_r vortices (centered at the origin)
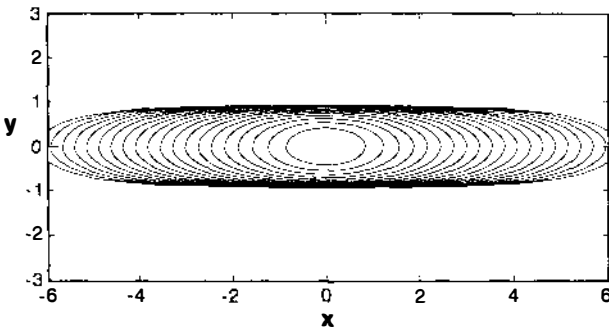

Figure 13 Boundaries of 20 different finite-L_r, potential vortices centered at the origin and embedded in $\bar{v}_x(y) = -\sigma_\bullet y$, where $\sigma_0/\tilde{q} = 0.5$. The family is band-like, so as A increases the vortices become flatter in shape and cannot extend in latitude past Y_{max}. From Equation (36) $Y_{max}/L_r = 1.145$. The unit of length in the figure is L_r.

can extend as $A \to \infty$ have been computed numerically as a function of $\sigma_0/\tilde{q}$ and are in good agreement with their asymptotic values (Marcus & Van Buskirk 1993):

$$Y_{\max} = L_r(3\tilde{q}/4\sigma_0)^{1/3}. \tag{36}$$

Equation (36) shows that for a wide range of $\bar{\sigma}/\tilde{q}$, the half height $Y_{\max}$ of a band-like vortex is of order L_r.

The Jovian weather layer has finite L_r and large $|\bar{\sigma}|$, so it should not be surprising that several Jovian vortices look band-like, particularly the anti-cyclonic Little Red Spot at 19°N (which is the location of the strongest anti-cyclonic $\bar{\sigma}$ on the planet), the very elongated cyclones at 30°S (Figure 4), and the four cyclonic barges with $\lambda \simeq 4$ at 14°N. Like the vortices in Figure 13, the λ of the barges increases with their areas (Mac Low & Ingersoll 1986). If the barges were Moore-Saffman vortices with λ given by equation (24), then $\bar{\sigma}/\tilde{q}$ would have to be ~ 3; whereas the observed values are ~ 0.4—consistent with a family of band-like vortices. Sub-stituting the observed values of the half-heights of the barges into the left-hand side of Equation (36) implies that $L_r \ll 2000$ km at the barges. This suggests that the barges, which are different in appearance from the other Jovian cyclones, might lie deeper in the atmosphere. At lower depths the atmosphere is less stably stratified, and L_r is smaller.

Because of the screening effects of L_r, it should be no surprise that the north and south sides of a vortex can act independent of each other and that an asymmetric vortex can have a northern boundary that acts as a corner-like vortex and extends into the region of adverse shear and a southern boundary in prograde $\bar{\sigma}$ that acts as a band-like vortex, so that no matter how large A becomes the vortex is bounded to the south at $y = -Y_{\max}$. We argue in the next section that many Jovian vortices lie asymmetrically in their local $\bar{v}$ and are hybrids of the two types of vortices.

10.   DIRECTION OF VORTEX OVERFLOW, $\bar{v}(y)$, AND MULTIPLE VORTICES

There are many theories of how $\bar{v}(y)$ is formed; none are totally satis-factory. Several assume that the east-west winds are rooted deep in the interior and not the weather layer (Ingersoll & Pollard 1982, Busse 1983). Others argue that $\bar{v}(y)$ is shallow and due to an atmospheric resonance (Mayr et al 1984), barotropic turbulence (Williams 1985), or thermal forcing (Conrath & Gierasch 1984).

Rhines & Young (1982) found that turbulent QG flows often form distinct domains of nearly uniform q. Here we outline our extension of these ideas to $\bar{v}$ because it explains the direction (pole or equator side) that

vortices overflow their zones or belts and also why some latitudes have more than one vortex. In this picture $\bar{v}$, like the vortices, is governed by the shallow-water potential vorticity Equation (1) of the weather layer and tied only weakly to the interior velocity by $h_b(y)$. Experiments and numerical simulations (Nielsen & Schoeberl 1984) suggest that if the weather layer is vigorously stirred it can form axisymmetric bands of approximately uniform q separated by thin regions where q changes rapidly. For example east-west flows with either one or two approximately axisymmetric bands of nearly uniform q were created in a rotating tank with a nonporous lid (Sommeria et al 1988, 1989) when the flow was stirred by injecting fluid in and out of holes in the bottom [exploiting the $(q/H_0)(\partial v_z/\partial z)$ forcing discussed in Section 3.1]. Numerical calculations of flows that are stirred by the axisymmetric injection and withdrawal of fluid at several radial locations quickly produce extrema in q at those locations. There the flow has local instabilities (as allowed by the inflection theorem) which mix the flow. If the forcing is sufficiently large the $\bar{v}$ can form distinct bands each with a nearly uniform q. The size, location, number, extent of the homogenization of q within the bands, and sharpness of the transition regions depend on the rate of injection, the dissipation, L_r, and the flow history. For example, when the forcing is weak it is hard to create bands greater than $2L_r$ in width. This method of creating a banded $\bar{v}(y)$ could apply to the Jovian weather layer if the rising and falling plumes in the underlying convection layer inject and withdraw fluid at several different latitudes (Stone 1976), and if the stably stratified overlying layer acts as a nonporous lid.

To see what types of east-west winds would be created by the forcing, assume that v was initially zero in the Jovian weather layer. Then $q(y) \equiv f(y) + f_0 h_b(y)/H_0 \simeq f(y)$, and $q(y)$ decreases monotonically from the north to south pole. If stirring mixed the q into approximately uniform bands, then $\bar{q}(y)$ would form a monotonically decreasing set of steps from the north to south pole. Moreover, if the average $\bar{v}$ and $\bar{\omega}$ of the resulting flow in each hemisphere remained approximately zero, then the $\bar{v}(y)$ would look qualitatively like the solid curve in Figure 1: The $\bar{v}(y)$ would be continuous, but $d\bar{v}(y)/dy$ and $\bar{q}$ would be nearly discontinuous at the band boundaries. [For example if within the ith band, $f(y) + h_b(y)f_0/H_0$ could be approximated as $f_0^i + \beta^i y$, then within each band $\bar{v}^i(y) = V_i \cosh [(y - y_i)/L_r] + k_i$ where V^i, y^i, and k^i are constants for each band.] The curve in Figure 1 fits v_{Lim} because the number of bands, their widths, values of q, and $h_b(y)$ are all adjustable parameters, but despite the arbitrariness in selecting these values the model has important implications. Each band contains one anti-cyclonic zone and one cyclonic belt with the belt always on the equatorial side. The east-going extrema of $\bar{v}(y)$ occur at band

boundaries where $\bar{q}(y)$ and $\bar{\sigma}(y)$ are almost discontinuous and $|\bar{\sigma}|$ is large. The west-going extrema are within the bands and have continuous $\bar{q}(y)$ and $\bar{\sigma}(y)$ with $\bar{\sigma} = 0$.

Regardless of what physical mechanisms makes the bands (we now define a band as one zone/belt pair with the zone on the pole side), our calculations show that prograde vortices can grow by merger until they overflow into the neighboring belt or zone within the same band but not across band boundaries if at the boundary there is a very rapid change in $\bar{q}$ or if $|\bar{\sigma}/\tilde{q}|$ is large. The overflowing vortices are hybrids. The side near the band boundary stretches in the east-west direction, stops growing in latitude, and acts as a band-like vortex. The other side near the middle of the band, easily overflows the zone-belt boundary where $\bar{\sigma} = 0$, and acts as a corner-like vortex. Thus a characteristic of this model of $\bar{v}(y)$ is that if there is vortex overflow into adverse $\bar{\sigma}$, then the cyclones overflow on the pole side and anti-cyclones on the equator side. This characteristic is true for all of the long-lived Jovian vortices. It is especially obvious in the *Voyager* photographs of the GRS, the three White Ovals, and the 24 vortices at 41°S (Figure 4).

A consequence is that an anti-cyclone can overlap in latitude and interact with the cyclones in the neighboring belt on its equatorial side (i.e. within the same band) but not with the cyclones on its poleward side (where their separations in latitude are usually greater than L_r). We can use this to explain how several Jovian vortices can co-exist all centered at the same latitude. An explanation is required because an isolated row of prograde QG vortices embedded in an east-west flow with approximately uniform q is always linearly unstable. The vortices approach each other and then merge together to form one large vortex, usually with some very small unmerged fragments (cf the late-time merger of the three White Ovals into one vortex in the simulation by Dowling & Ingersoll 1989). Observations of the White Ovals show that when they begin to approach each other they are pushed back to their original locations with a repulsion that increases inversely with the square of their separations (Solberg 1969). We can prevent the vortices in a row from approaching each other (thereby blocking merger) by introducing a second staggered row of opposite-signed, prograde, *blocking* vortices as in Figure 4 or schematically as in Figure 14.

A pair of staggered rows of opposite-signed vortices is called a Kármán vortex street. Its eigenmodes can be found numerically, but when the vortices are point potential vortices and $L_r \to \infty$ they can be found in closed form (Lamb 1932, Marcus 1990) and when $a \gg L_r$ they can be computed approximately by considering a perturbed vortex's response to $\bar{v}(y)$ and the $\tilde{v}$ of its nearest neighbors. First consider the stability of the bottom
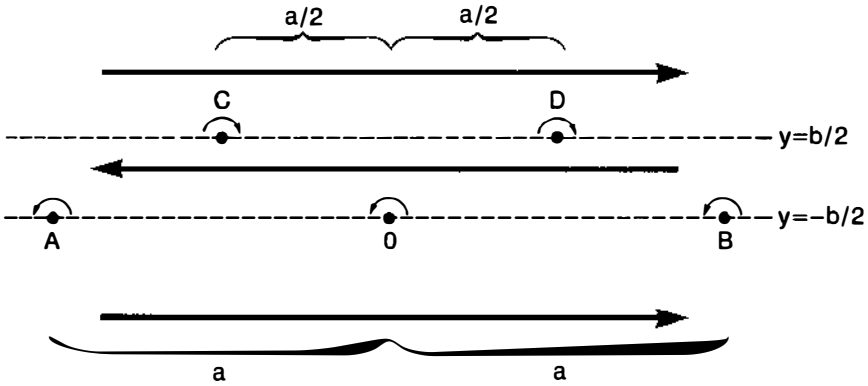
Figure 14 Schematic of a row of point potential vortices with circulations $-\tilde{\Gamma}$ above and staggered with a row of vortices with circulation $\tilde{\Gamma}$ (Kármán vortex street). The $\bar{\mathbf{v}}(y)$ is shown with heavy arrows and the $\tilde{\mathbf{v}}$ with thin. The figure is in the moving frame such that at equilibrium the vortices are at rest. Note that at the latitudes of the rows of vortices $\bar{\mathbf{v}} \neq 0$.

row of prograde vortices with potential circulation $\tilde{\Gamma}$ in Figure 14 without the second row at $y = b/2$. Let vortex **O** be perturbed upward a distance δ from its equilibrium. Neighboring vortices **A** and **B** and $\bar{\mathbf{v}}$ move **O** to the left with linearized velocity $[\bar{\sigma}(-b/2) + d^2\tilde{\psi}/dy^2]\delta$ where the derivative is evaluated at the equilibrium position of **O** and the $\tilde{\psi}$ due to **A** and **B** is calculated from Equation (10). After vortex **O** moves to the left, it is advected upward by vortex **A**, moving it even farther from its equilibrium latitude. There is no restoring force, the row is unstable, and vortices **O** and **A** quickly move to the same longitude where they would merge if they were of finite size. When the row of vortices at $y = b/2$ with circulations $-\tilde{\Gamma}$ is included, the perturbed vortex **O** can move to the left or right. For values of the parameters relevant to Jupiter, $a \gg b \sim L_r$, and $|\bar{\sigma}(\pm b/2)| \sim \tilde{\Gamma}/\pi ab$, the perturbed velocity $\bar{\sigma}(-b/2)\delta$ due to $\bar{\mathbf{v}}$ dominates the perturbed $\tilde{\mathbf{v}}$, so **O** still moves to the left. ($\tilde{\Gamma}/\pi ab$ is approximately the $\tilde{q}$ of the finite-area potential vortices in Figure 4.) Then the downward $\tilde{v}_y$ on **O** created by the close proximity of **C** exponentially dominates the influence of **A**, **B**, and **D**, so **O** moves downward and south of latitude $y = -b/2$ where it is then advected to the right. It then completes a counterclockwise orbit around its old equilibrium position. The counterclockwise motion is consistent with the numerically computed eigenmode, and the period of the orbit is consistent with the numerically computed neutrally stable eigenvalue. Note that for different values of the parameters or large initial perturbations the staggered rows of vortices can be unstable.

Thus another characteristic of the model is that if there are $N > 1$ long-

lived prograde anti-cyclones centered at some latitude, then they must be part of a Kármán vortex street with N blocking cyclones in the belt on the equatorial side (i.e. within the same band); otherwise the vortices will merge. Due to Jovian turbulence it is unlikely that a Jovian vortex street would oscillate exactly periodically in time or that its vortices would be equally spaced. A Jovian vortex street is clearly located at 41°S where there are nine well-formed, staggered, cyclone/anti-cyclone pairs spanning 205° in longitude (Figure 4) and three other less distinct pairs in the remainder. The three White Ovals form a vortex street with the three very extended, weak cyclones at 30°S (Figure 3). There are also striking examples of vortex streets in the North such as the one at 44.5°N. Vortices in these streets have not been observed to merge or disappear. Because the cyclones are usually located near the anti-cyclones, some observers have claimed that they are the wakes of anti-cyclones [i.e. passive consequences of the anti-cyclones rather than dynamically important blocking vortices that create the oscillations observed by Solberg (1969)]. However, it should be noted that all three of the White Ovals and two of their companion cyclones lie within a 180° span of longitude, leaving one cyclone spatially isolated and clearly not a wake. The observations are not sufficiently complete to determine whether there are blocking vortices present in all examples of two or more, long-lived Jovian vortices occupying the same latitude; however, observations of vortex mergers are very common when there are no blocking vortices, cf the anti-cyclones at 35°N.

The GRS is an example of a vortex with no companion at its latitude. If blocking vortices are the only way to prevent vortices at the same latitude from merging, then for the GRS to have a companion there would have to be a blocking cyclone in the belt north of 17°S. There is none [possibly because that belt has a strong 3-dimensional flow (as indicated by regions of intense convection) that is not conducive to robust 2-dimensional vortices]. Another property of QG vortex arrays embedded in east-west flows with approximately uniform q is that when the two rows of point vortices are not staggered as in Figure 14, but directly over each other (so the vortices looked like dipolar modons), they are unstable. So though vortex dipoles are common in many geophysical flows, they should not exist on Jupiter. This is consistent with observations.

Nezlin (1986) has a different explanation for why some Jovian latitudes have more than one vortex. He has concluded that the Jovian zone-belt flow is linearly unstable to IG eigenmodes of the form $e^{im\phi}$, where ϕ is the longitude and m is an integer and a local function of the latitude. He argues that the number of observed vortices at each latitude is equal to m. A problem with this reasoning is illustrated in Figure 7. Here the $\bar{v}$ is most linearly unstable to $m = 3$, and although the flow is initially dominated by

the wavenumber $m = 3$ of the linear instability, the final number of vortices, in this case one, depends on how many survive the subsequent nonlinear mergers. Moreover as noted by Williams & Wilson (1988) who carried out numerical simulations of IG vortices, in order to maintain multiple IG vortices at the same latitude there must be a delicate balance so that they all move at the same speed (otherwise one catches up with another and they merge). It would be unlikely that such a balance could be maintained in the turbulent Jovian atmosphere.

11. VELOCITY DATA

Jovian velocity vectors are derived from *Voyager* photographs by identifying cloudlets, looking at their displacements over time τ (usually a Jovian day), and dividing by τ. This assumes that the clouds move with $\mathbf{v}$, have accelerations small compared to $\langle v \rangle / \tau$, have displacement lengths small compared to the flow's radius of curvature, are all at the same altitude, and have precisely known locations. Satellite pointing problems cause large uncertainties in the latter unless photographs of the cloudlet and planet's limb can be overlapped. Mitchell et al (1981) and R. F. Beebe (1991, private communication) have determined several thousand cloudlet displacements in the GRS. To reduce their noise, Dowling & Ingersoll (1989) averaged them over $3 \times 3°$ ($\sim 3450 \times 3450$ km) cells (i.e. 9×5 cells over the GRS). The values of $\mathbf{v}$ and their first derivatives for each cell were found by fitting the observed velocities within each cell to a linear function of latitude and longitude. Their goal was to use the smoothed $\mathbf{v}$ and ω in the steady-state shallow-water equations to solve for $h_b(y)$. To examine the effects of smoothing, Van Buskirk (1991) used a thin shell, 2-dimensional spline on the Beebe displacements to obtain $\mathbf{v}$ on a $0.39°$ or ~ 450 km square grid. The unsmoothed energy spectrum has an unreasonably large peak at the large wavenumber $\mathbf{k}$ Fourier modes; moreover, spatial derivatives (e.g. ω) of the unsmoothed $\mathbf{v}$ are dominated by the noise at large $\mathbf{k}$. We smoothed $\mathbf{v}$ by Gaussian filtering in Fourier space, and computed $\mathbf{v}$ and ω as functions of smoothing length L. We found that $\mathbf{v}$ varied by 13% and ω by 28% as L was changed from $1°$ to $3°$. This is not surprising when one considers the GRS in Figure 2 superposed with a $3 \times 3°$ grid. The thin circumferential ring of high velocity of width $\sim 2L_r$ (Figure 3) almost falls between the grid points. Inside the ring, ω exponentially increases with e-folding length of $2°$ from near zero to its peak value, drops back to zero, reaches its most negative value, and then exponentially returns to near zero. When the smoothing distance is larger than the e-folding length, errors of 20–40% should be expected in the velocity derivatives. Functions of higher derivatives, such as h_b as calculated by Dowling & Ingersoll

(1989), which depend on the spatial variation of ω, are even more inaccurate. For these reasons we do not believe the published values of h_b that were derived from the 3°-averaged $\mathbf{v}$.

We can use Beebe's displacements to test the validity of the shallow-water approximation by using a modification of a method used to reduce noise in experimental measurements of a flow which should be exactly 2-dimensional and divergence-free but in which the noise causes $\nabla \cdot \mathbf{v} \neq 0$. This noise filter finds the projection $\mathbf{v}_{proj}$ of $\mathbf{v}$ onto the set of 2-dimensional, divergence-free fields with the same (periodic or zero normal component) boundary conditions as $\mathbf{v}$ such that the L_2 norm of $(\mathbf{v}_{proj} - \mathbf{v})$ is minimized. To do this we compute ω from the smoothed $\mathbf{v}$, calculate ψ such that $\nabla^2 \psi \equiv \omega$. We define $\mathbf{v}_{proj} \equiv \hat{\mathbf{z}} \times \nabla \psi$ (where ∇^2 is inverted with appropriate boundary conditions). If the Beebe displacements of the GRS obey the shallow-water equations, we should not constrain them to be divergence-free. Instead we compute a $\mathbf{v}_{proj}$ by projecting them onto the set of 2-dimensional fields that exactly satisfy the steady-state, shallow-water momentum Equation (1). (In the limit $f \to f_0$ and $\varepsilon \to 0$ this projection would be identical to the previous one: $\nabla \cdot \mathbf{v}_{proj} = 0$ with $\psi = gh/f_0$.) The divergence of Equation (1) gives gh in terms of the smoothed $\mathbf{v}$:

$$\nabla^2 gh = \nabla \cdot [\mathbf{v} \times f\hat{\mathbf{z}} - (\mathbf{v} \cdot \nabla)\mathbf{v}] \tag{37}$$

and the Laplacian is inverted to find gh. Then $\mathbf{v}_{proj}$ is defined as

$$\mathbf{v}_{proj} \equiv \hat{\mathbf{z}} \times \frac{1}{f}[g\nabla h + (\mathbf{v}_{proj} \cdot \nabla)\mathbf{v}_{proj}] \tag{38}$$

so $\mathbf{v}_{proj}$ exactly satisfies the steady-state form of Equation (1). [Equation (38) is the analog of $\mathbf{v}_{proj} \equiv \hat{\mathbf{z}} \times \nabla \psi$.] Equation (38) can be solved iteratively with linear convergence in the Rossby number by defining the $(n+1)^{st}$ iterate:

$$\mathbf{v}_{proj}^{n+1} \equiv \hat{\mathbf{z}} \times \frac{1}{f}[g\nabla h + (\mathbf{v}_{proj}^n \cdot \nabla)\mathbf{v}_{proj}^n]. \tag{39}$$

The L_2 difference between $\mathbf{v}_{proj}$ and the 1°-smoothed velocity is less than 7%, which is within the observational uncertainties, and which justifies, in part, the shallow-water approximation. In particular, it shows that the data are consistent with a steady state momentum equation in which there are no baroclinic terms.

Although the $\mathbf{v}_{proj}$ and the $\mathbf{v}$ computed from smoothing over 1° are nearly the same, the values of $\nabla \cdot \mathbf{v}$ and h_b derived from these two velocities differ by order unity. They are very sensitive to small changes in $\mathbf{v}$. For this reason we have computed $h_b(y)$ with an alternative method. We assume that the potential vorticity of the Limaye velocity $q_{Lim} \equiv H_0[f(y) +$

$\omega_{\text{Lim}}(y)]/[H_0+h_{\text{Lim}}(y)-h_b(y)]$ is uniform over some band, where h_{Lim} is defined so that it and v_{Lim} exactly satisfy the steady shallow-water momentum Equation (1) or

$$gh_{\text{Lim}}(y) = -\int_{y_*}^{y} v_{\text{Lim}}(y')f(y')\,dy', \tag{40}$$

where y_* is chosen such that $(h_{\text{Lim}})_0 \equiv 0$, and where $(\ )_0$ means an average over the band where q_{Lim} is assumed constant. Thus

$$gh_b(y) = gh_{\text{Lim}}(y) - L_r^2 f_0^2 \frac{[f(y)-f_0]+[\omega_{\text{Lim}}(y)-(\omega_{\text{Lim}})_0]}{f_0+(\omega_{\text{Lim}})_0}, \tag{41}$$

where we have defined $h_b(y)$ such that $(h_b(y))_0 \equiv 0$. There are order unity differences between the $h_b(y)$ found from Equation (41) and that found by Dowling & Ingersoll. When the former is used in an initial-value calculation that begins with v_{proj}, the flow remains nearly unchanged over time. In contrast, when Dowling & Ingersoll used the latter h_b and initialized their calculation with v_{Lim}, they found that the flow was unstable at the latitude of the GRS: Waves formed and rolled up into vortices that then merged together much like the unstable vortex layer does in Figure 7. They interpreted their numerical experiment as a scenario for the formation of the GRS as well as support for their values of $h_b(y)$. A different point of view is that the observed Limaye velocity should be compared with the *final* state of a numerical experiment and not just used as its *initial* state. In the experiment of Dowling & Ingersoll, the final east-west flow (far from the GRS) differs from v_{Lim} by as much as 20% at some latitudes. Moreover, if the observed $v_{\text{Lim}}(y)$ (which at most locations is much farther than L_r from the GRS and any possible stabilizing influence it might have) is found to be unstable with respect to some choice of $h_b(y)$, we argue that that choice of h_b is incorrect.

With $L_r = 2300$ km we have found that $\langle|\tilde{h}/H_0|\rangle \sim 0.18$ (using h derived from Equation 37), $\langle|h_b/H_0|\rangle \sim 0.12$ (using the h_b from Equation 41), and over most of the GRS $\langle\omega/f_0\rangle$ is less than 0.2, all consistent with QG scaling. The value of $\tilde{h}/H_0$ and its behavior can be understood by noting that $\tilde{v}$ is nearly zero everywhere except on the circumferential ring; therefore, its stream function $g\tilde{h}/f_0$ is nearly constant inside and outside the GRS. By definition $\tilde{h} \simeq 0$ outside the GRS. The ring thickness is $\sim 2L_r$, so the maximum value of $\tilde{h}$ is at the center of the GRS and is $2L_r$ times $|\nabla\tilde{h}|$ in the ring. Equation (5) or geostrophy requires $|\nabla\tilde{h}| \simeq f_0|\tilde{v}|/g$, so the maximum value of $\tilde{h}/H_0$ is $\sim 2\langle\tilde{v}\rangle/L_r f_0$. Because the latitudinal extent of the GRS is large, $\langle f(y)-f_0\rangle/f_0$ can be as large as 0.34, and at the nothernmost part of the circumferential ring $|\omega/f_0|$ is as large as 0.35. These

difficulties are discussed below, but we note here that only two conditions need to be satisfied to derive the QG equations from the shallow-water equations:

$$f_0^2 L_r^2 (f+\omega)/g(H_0+h-h_b) \simeq f+\omega+g(h_b-h)/f_0 L_r^2 \qquad (42)$$

and

$$f_0 \mathbf{v} \simeq g\hat{\mathbf{z}} \times \nabla h. \qquad (43)$$

For the GRS, Williams & Yamagata (1984) rejected QG in favor of IG theory which assumes the shallow-water approximations and the additional scalings: $\langle v \rangle/|f_0|\langle l \rangle = \langle [f-f_0]/f_0 \rangle^2 = (L_r/\langle l \rangle)^2 \ll 1$. They reasoned that $L_r = 2000$ km and $\langle l \rangle = 17{,}000$ km, the latter being the average radius of the GRS, so $(L_r/\langle l \rangle)^2 \ll 1$. However, $\langle l \rangle$ should be the characteristic distance over which h and $\mathbf{v}$ change (which is order L_r) not the size of the GRS (Marcus et al 1990).[7] Williams & Yamagata argue that $\langle \omega \rangle/f_0 = [v]/|f_0|\langle l \rangle$ and $\langle h \rangle/H_0 = \langle l \rangle\langle v \rangle/|f_0|L_r^2$. However, by identifying $\langle l \rangle$ as 17,000 km rather than the distance over which $\mathbf{v}$ changes, they conclude that $\langle \omega \rangle/f_0 = 0.02$ [which is a factor of 10 smaller than the measured values (Dowling & Ingersoll 1989, Van Buskirk 1991)] and $\langle h \rangle/H_0 = 1.4$ (which is a factor of 10 too big). The *Voyager* data do not support the IG scaling.

A valid criticism of the QG approximation for the GRS is that $[f(y)-f_0]/f_0$ and $\langle \mathbf{v} \rangle/|f_0|\langle l \rangle$ can be as large as 0.35. However these problems can be overcome with a more generalized QG theory by writing the shallow-water potential vorticity Equation (2)

$$H_0 \frac{D}{Dt}\left(\frac{\omega+f}{H}\right) \equiv \frac{D}{Dt}\bar{q}\left[\frac{1+\dfrac{\tilde{\omega}}{f+\tilde{\omega}}}{1+\dfrac{\tilde{h}}{H_0+\bar{h}-h_b}}\right] \simeq$$

$$\frac{D}{Dt}\left[\frac{\tilde{\omega}(x,y,t)}{f(y)+\tilde{\omega}(y)} - \frac{\tilde{h}(x,y,t)}{H_0+\bar{h}(y)-h_b(y)}\right] = 0, \quad (44)$$

where $\bar{q}$ and $\bar{h}$ are the q and h of $\bar{\mathbf{v}}$, and where $\bar{h}$ is constructed so that it and $\bar{\mathbf{v}}$ exactly satisfy the steady shallow-water Equation (1). Equation (44) uses the definition that $\bar{q}$ is constant and the assumptions that $[\tilde{h}/(H_0-h_b+\bar{h})] \ll 1$ and $[\tilde{\omega}/(f+\tilde{\omega})] \ll 1$. It does not require that $[f(y)-f_0]/f_0$ be small nor does it require that $\bar{\mathbf{v}}$ be QG. For the GRS,

---

[7] The only time $\langle l \rangle$ should be identified with the size, or latitudinal extent of the GRS is if one estimates $\langle f-f_0 \rangle$ as $\beta\langle l \rangle$.

$|\tilde{\omega}/(f+\tilde{\omega})|$ and $|\tilde{h}/(H_0-h_b+\tilde{h})|$ are everywhere less than 0.2. With these same assumptions, Equation (1) gives a linear, homogeneous, elliptic relation between $\tilde{h}$ and $\tilde{\omega}$ that is the analog of the QG relation $\tilde{\omega} = \nabla^2 g\tilde{h}/f_0$. So there is still a Greens function that relates $\tilde{h}$ with $\tilde{q}$, but it is no longer a Bessel function. Because the potential vorticity that is advected by Equation (44) is homogeneous and linear in $\tilde{h}$, all of the techniques used in QG theory—point potential vortices, contour dynamics, velocities of patches of q, etc—also work for generalized QG theory, as do all of the qualitative arguments—expulsion of adverse vorticity, stability of staggered rows of vortices, slowly rotating centers, etc.

12.   CONCLUSIONS

We have shown that Jovian vortices reflect the behavior of quasi-geostrophic (QG) vortices embedded in an east-west wind with bands of uniform potential vorticity. Jovian vortices certainly have some non-QG components and baroclinicity, and the bands must have some gradient of their potential vorticities (otherwise there would be no Rossby waves). These effects must be included to make quantitative comparisons between observation and theory. Yet this paper argues that most of the properties of the Jovian vortices can be easily explained and understood with QG theory. Many of the signatures of QG vortices are apparent in *Voyager* images. Robust QG vortices, like Jovian vortices, regardless of whether they are anti-cyclones or cyclones, are always prograde with respect to their surrounding shear $\bar{\sigma}$. Potential vorticity $\tilde{q}$ is attracted to prograde zones and belts and is expelled from adverse shear. Many linearly stable, prograde QG vortices are also stable to large perturbations; if one is broken apart by turbulence, it often reforms because prograde vortices at or near the same latitudes tend to merge together. There are no (known) steady adverse vortices for $|\bar{\sigma}/\tilde{q}| \sim O(1)$, and for small $|\bar{\sigma}/\tilde{q}|$ adverse vortices are unstable to small perturbations. Continual accretion of small area, large $|\tilde{q}|$ vortices can maintain large, weakly dissipative vortices such as the GRS. The merger of two prograde vortices near the same latitude lowers their energy, but if the initial latitudinal separation increases beyond a critical value, their energy increases. Vortices tend to merge when their initial separation is less than the critical value. It is easier for vortices to merge with $\bar{\sigma}$ than it is without it because the differential east-west velocity $\bar{v}(y)$ pushes vortices together and because it breaks the angular momentum barrier and other kinematic constraints that prevent vortices from approaching each other. Because the QG equations advectively conserve potential vorticity, QG and Jovian vortices move with the local ($\tilde{q}$-

weighted) $\mathbf{v}$ which is approximately the same as the local east-west, zone-belt velocity.

In numerical and laboratory experiments, QG vortices relax to approximately steady states like the Jovian vortices, rather than oscillating or rotating Kida ellipses. Prograde QG vortices with characteristic radii R much less than L_r have shapes with aspect ratios that scale with $\bar{\sigma}/\tilde{q}$ like the Moore-Saffman vortices, but when corner-like vortices overflow into regions of adverse shear their northern or southern boundaries pucker towards the stagnation points. For $R \gg L_r$, band-like vortices become very elongated in the longitudinal direction, like the cyclonic barges at $14°N$. Many Jovian vortices like the GRS and the White Ovals are hybrids with the equatorial side of anti-cyclones acting corner-like and the pole side band-like. The size of QG vortices is determined by the widths of the belts or zones in which they lie, though the limiting mechanism—collision with a stagnation point, loss of stability, or flattening due to large prograde shear—depends on L_r and whether the vortices are band-like or corner-like.

In numerical experiments large vortices built by the merger of many small ones have nearly uniform $\tilde{q}$. The hallmark of a uniform-q, QG vortex with $R \gg L_r$ is that its velocity and vorticity ω are concentrated in a circumferential ring around it leaving the interior almost irrotational. The $\mathbf{v}$ and $|\omega|$ increase exponentially outward from the center with e-folding length L_r. The ring thickness is $\sim 2L_r$. If $|\tilde{q}|$ is not exactly uniform but increases outward from the vortex center with its critical gradient (for linear stability), the concentration of $\mathbf{v}$ and ω in the ring is even greater. (It is still speculative whether accreting, dissipative vortices have critical gradients.) The concentration of $\mathbf{v}$ and ω in the ring decreases as R/L_r decreases, and in the limit $L_r \to \infty$, $\bar{\sigma} \to$ constant, there is no differential rotation within the vortex. The concentration of $\mathbf{v}$ into a ring is obvious in the GRS, and its decrease with R/L_r is apparent in the White Ovals. The signature of IG vortices is different; ω is Gaussianly peaked at the vortex center.

When approximately axisymmetric bands of nearly uniform q form in numerical experiments with forcing and dissipation they have an anti-cyclonic zone on the pole side and a cyclonic belt on the equator side. Hybrid vortices often overflow the zone-belt boundary within the band but not across band boundaries, so cyclones overflow towards the pole and anti-cyclones like the GRS and White Ovals towards the equator. In the absence of contrived boundary conditions, forcing, or dissipation, and in the presence of turbulence, the only way now known to prevent multiple anti-cyclones at the same latitude from approaching and merging with each other is to place a staggered row of N blocking cyclones between

them in a neighboring belt. If L_r is of order or smaller than the width of the zone and if the vortices are hybrids, the cyclones and anti-cyclones must be within the same band and the cyclones must be on the equator side of the anti-cyclones. The best Jovian example of staggered rows of cyclones and anti-cyclones is at 41°S. The flow on the equator side of the GRS is three-dimensional and turbulent. It does not support long-lived blocking vortices. Thus there are no other vortices at the same latitude as the GRS.

Cyclones and anti-cyclones are not dynamically different in QG theory (unless the belts and zones differ). However, the appearance of the clouds in Jovian vortices (filamentary, with no relation between their edges and the stream function for many cyclones, or smooth ellipses surrounded by a cloud-free ring for anti-cyclones) can be better explained by changing the locations where clouds are created or destroyed (which is different for cyclones and anti-cyclones due to Ekman pumping) rather than by any intrinsic differences between the velocities of cyclones and anti-cyclones.

Clearly, all of the properties of Jovian vortices cannot be derived from just the QG or any other model equations. The number of vortices that survive merger within each band is very sensitive to initial conditions. Moreover, the Jovian weather layer is much more turbulent with fewer vortices in the north than it is in the south, and this must be due either to a physical asymmetry of the boundary or initial conditions. Some of the results presented here are still speculative, and more work needs to be done, especially in developing a self-consistent model that accounts for both the east-west winds and the vortices. Unlike the time-reversible shallow-water and QG equations, the model should include the effects of thermal convection, Rossby radiation, etc, so that the simulated Jovian flows are a dynamic equilibrium of the forces and dissipation.

Literature Cited

Antipov, S. V., Nczlin, M. V., Snezhkin, E. N., Trubnikov, A. S. 1982. *Sov. Phys. JETP* 82: 145–60

Beebe, R. F., Orton, G. S., West, R. A. 1989. In *Time-Variable Phenomena in the Jovian System*, ed. M. J. S. Belton, R.

A. West, J. Rahe. NASA SP-494

Busse, F. H. 1983. *Geophys. Astrophys. Fluid Dyn.* 23: 153–74

Cassini, C. F. 1666. *Philos. Trans. R. Soc. London* 1: 143

Chorin, A. J. 1993.. *Vorticity and Tur-*

bulence. New York: Springer-Verlag

Conrath, B. J. Gierasch, P. J. 1984. *Icarus* 57: 184–204

Dowling, T. E., Ingersoll, A. P. 1989. *J. Atmos. Sci.* 46: 3256–78

Dritschel, D. G. 1988. *J. Comput. Phys.* 77: 240–66

Flaser, F. M., Conrath, B. J., Pirraglia, J. A., Clark P. C., French, R. G., Gierasch, P. J. 1981. *J. Geophys. Res.* 86: 8759–67

Flierl, G. R., Stern, M. E., Whitehead, J. A. Jr. 1983. *Dyn. Atmos. Oceans* 7: 233–63

Ghil, M., Childress, S. 1987. *Topics in Geophysical Fluid Dynamics: Atmospheric Dynamics, Dynamo Theory, and Climate Dynamics. Appl. Math. Sci. Ser.* 60. New York: Springer-Verlag

Golitsyn, G. S. 1970. *Icarus* 13: 1–24

Hanel, R., Conrath, B., Flaser, M., Herath, L., Kunde, V., et al. 1979. *Science* 206: 952–56

Hatzes, A., Wenkert, D. D., Ingersoll, A. P., Danielson, G, E. 1981. *J. Geophys. Res.* 50: 3517–20

Hook, R. 1665. *Philos. Trans. R. Soc. London* 1: 3

Hunt, G. E. 1983. *Annu. Rev. Earth Planet. Sci.* 11: 415–59

Ingersoll, A. P. 1990. *Science* 248: 308–15

Ingersoll, A. P. Cuong, P. G. 1981. *J. Atmos. Sci.* 38: 2067–76

Ingersoll, A. P., Pollard, D. 1982. *Icarus* 52: 62–80

Kida, S. 1981. *J. Phys. Soc. Jpn.* 50: 3517–20

Lamb, H. 1932. *Hydrodynamics.* Cambridge: Cambridge Univ. Press

Limaye, S. S. 1986. *Icarus* 65: 335–52

Mac Low, M.-M., Ingersoll, A. P. 1986. *Icarus* 65: 353–69

Marcus, P. S. 1986. In *Numerical Analysis. Proc. Conf. of June 1985, Dundee, Scotland,* ed. D. F. Griffiths, G. A. Watson, pp. 125–39. Edinburgh: Longman

Marcus, P. S. 1988a. *Nature* 331: 693–96

Marcus, P. S. 1988b. *Nucl. Phys. B* Proc. Suppl. 2: 127–38

Marcus, P. S. 1990. *J. Fluid Mech.* 215: 393–430

Marcus, P. S., Graves, C. 1993. *Icarus.* In preparation

Marcus, P. S., Sommeria, J., Meyers, S. D., Swinney, H. L. 1990. *Nature* 343: 517–18

Marcus, P. S., Van Buskirk, R. D. 1993. *J. Fluid Mech.* In preparation

Maxworthy, T., Redekopp, L. G. 1976. *Icarus* 29: 261–71

Mayr, H. G., Harris, I., Chan, K. L. 1984. *Earth Moon Planets* 30: 245–74

Mitchell, J. L., Beebe, R. F., Ingersoll, A. P., Garneau, G. W. 1981. *J. Geophys. Res.* 86: 8751–57

Moore, D. W., Saffman, P.G. 1971. In *Aircraft Wake Turbulence and its Detection,* ed. J. Olsen, A. Goldberg, N. Rogers. New York: Plenum

Nezlin, M. V. 1986. *Sov. Phys. Usp.* 29: 817–42

Nielsen, J. E., Schoeberl, M. R. 1984. *J. Atmos. Sci.* 41: 2869–81

Overman, E. A., Zabusky, N. J. 1982. *Phys. Fluids* 25: 1297–305

Polvani, L. M., Wisdom, J., DeJong, E., Ingersoll, A. P. 1990. *Science* 249: 1393–98

Pratt, L. J., Stern, M. E. 1986. *J. Phys. Oceanogr.* 16: 1101–20

Read, P. L., Hide, R. 1984. *Nature* 308: 45–48

Rhines, P. B., Young, W. R. 1982. *J. Fluid Mech.* 122: 347–67

Smith, B. A., Hunt, G. E. 1976. In *Jupiter,* ed. T. Gehrels, pp. 564–85. Tucson: Univ. Ariz. Press

Solberg, H. G. 1969. *Planet. Space Sci.* 17: 1573–80

Sommeria, J., Meyers, S. D., Swinney, H. L. 1988. *Nature* 331: 689–93

Sommeria, J., Meyers, S. D. Swinney, H. L. 1989. *Nature* 337: 58–61

Stevenson, D. J. 1982. *Annu. Rev. Earth Planet. Sci.* 10: 257–95

Stone, P. H. 1976. In *Jupiter,* ed. T. Gehrels, pp. 586–618. Tucson: Univ. Ariz. Press

Van Buskirk, R. D. 1991. *Quasi-geostrophic vortices in zonal shear.* PhD thesis. Harvard Univ.

Van Buskirk, R. D., Marcus, P. S. 1993a. *J. Comput. Phys.* Submitted

Van Buskirk, R. D., Marcus, P. S. 1993b. *J. Fluid Mech.* Submitted

Williams, G. P. 1985. *Adv. Geophys.* 28A: 381–428

Williams, G. P., Wilson, J. P. 1988. *J. Atmos. Sci.* 45: 207–41

Williams, G. P., Yamagata, T. 1984. *J. Atmos. Sci.* 41: 453–78